Quantum criticality on a chiral ladder: An SU(2) infinite density matrix renormalization group study

Philipp Schmoll,[1,2] Andreas Haller,[1,2] Matteo Rizzi,[1,3,4] and Román Orús[1,5,6]

[1]*Institute of Physics, Johannes Gutenberg University, 55099 Mainz, Germany*
[2]*Graduate School Materials Science in Mainz, Staudingerweg 9, 55128 Mainz, Germany*
[3]*Institute of Quantum Control (PGI-8), Forschungszentrum Jülich, D-52425 Jülich, Germany*
[4]*Institute for Theoretical Physics, University of Cologne, D-50937 Köln, Germany*
[5]*Donostia International Physics Center, Paseo Manuel de Lardizabal 4, E-20018 San Sebastián, Spain*
[6]*Ikerbasque Foundation for Science, Maria Diaz de Haro 3, E-48013 Bilbao, Spain*

In this paper we study the ground-state properties of a ladder Hamiltonian with chiral SU(2)-invariant spin interactions, a possible first step toward the construction of truly two-dimensional nontrivial systems with chiral properties starting from quasi-one-dimensional ones. Our analysis uses a recent implementation by us of SU(2) symmetry in tensor network algorithms, specifically for infinite density matrix renormalization group. After a preliminary analysis with Kadanoff coarse graining and exact diagonalization for a small-size system, we discuss its bosonization and recap the continuum limit of the model to show that it corresponds to a conformal field theory, in agreement with our numerical findings. In particular, the scaling of the entanglement entropy as well as finite-entanglement scaling data show that the ground-state properties match those of the universality class of a $c = 1$ conformal field theory (CFT) in $(1 + 1)$ dimensions. We also study the algebraic decay of spin-spin and dimer-dimer correlation functions, as well as the algebraic convergence of the ground-state energy with the bond dimension, and the entanglement spectrum of half an infinite chain. Our results for the entanglement spectrum are remarkably similar to those of the spin-$\frac{1}{2}$ Heisenberg chain, which we take as a strong indication that both systems are described by the same CFT at low energies, i.e., an $SU(2)_1$ Wess-Zumino-Witten theory. Moreover, we explain in detail how to construct matrix product operators for SU(2)-invariant three-spin interactions, something that had not been addressed with sufficient depth in the literature.

I. INTRODUCTION

The study of quantum criticality with density matrix renormalization group (DMRG) [1] has a long history. As such, quantum critical systems have an infinite correlation length, and it is well known that this cannot be exactly captured by DMRG, which is based on matrix product states (MPS) [2], but perhaps rather by other tensor networks [3] such as the multiscale entanglement renormalization ansatz [4] and tree tensor networks [5]. Nevertheless, DMRG is very efficient and simple to program, and this is the reason why often it is the preferred option to study criticality, both in its finite-size and infinite-size (iDMRG) [6] versions. The approach, then, is to push forward as much as possible the MPS bond dimension, and do appropriate finite-size and/or finite-entanglement [7] scalings to extract critical properties. To push the bond dimension, one of the best ideas is to implement symmetries. In particular, for SU(2)-invariant systems, the use of SU(2) at the level of the MPS has proven remarkably useful in simulations of, e.g., Heisenberg quantum spin chains and quasi-one-dimensional (quasi-1D) systems [8].

In this paper we use our own implementation of SU(2)-invariant iDMRG [9] to study the ground-state properties of a spin-$\frac{1}{2}$ two-leg ladder with chiral three-spin interactions. The model is similar to the system in Ref. [10], defined on the two-dimensional kagome lattice and with a Hamiltonian

made of purely chiral three-spin terms.[1] In that model, a ground-state analysis using two-dimensional (2D) DMRG in cylinders unveiled a ground state with chiral topological order. Here, our motivation for studying the ladder is multifold. First, it allows us to study the crossover from 1D to 2D for chiral interactions. In particular, we find that the ladder has chiral properties similar to those of the chiral edge mode in the 2D model, and a critical ground state with a central charge $c = 1$ and other critical exponents that we characterize numerically. Our findings are also compatible with previous studies showing that the continuum limit of the model is a $(1 + 1)$-dimensional conformal field theory (CFT) [11–13], and show in particular that the entanglement spectrum matches the expected behavior of an $SU(2)_1$ Wess-Zumino-Witten (WZW) theory at low energies. Moreover, the technical simulation of the model allows us to understand how to implement SU(2)-invariant matrix product operators (MPO) for Hamiltonians with three-spin chiral interactions, something that, to our surprise, had not yet been discussed with enough detail in the literature. Finally, the model is one of

---

[1]Here, we use the word "chiral" in the sense that the Hamiltonian is not even under a time-reversal operation. As we will see later, the continuum limit is a field theory which is odd under time reversal.
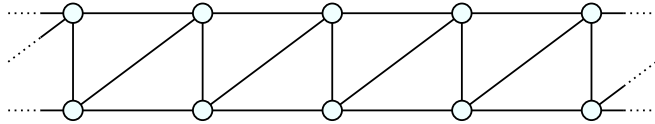
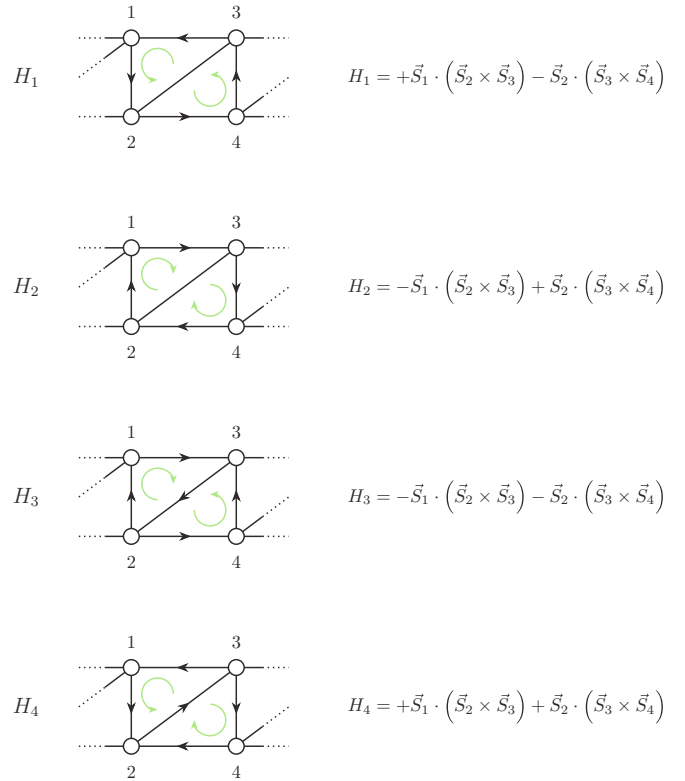FIG. 1. Two-leg ladder made of triangles, for the model in Eq. (1).

FIG. 2. Different orientations of the chiral triple product result in different models. In the first two cases, the orientation is chosen to be the same whereas it is opposite in the last two cases.

the simplest SU(2) generalizations of a quite widespread strategy in trying to access nontrivial two-dimensional systems with chiral properties, starting from quasi-one-dimensional ones (often dubbed as "wire deconstructionism") [14,15]: the key idea being to gap out right movers of a wire with left movers (or vice versa) of the neighboring one by means of suitable interactions, remaining at the end with a chiral edge current on the external legs of the ladder. Such an approach is experiencing a growing application in cold atoms, photonics, and nanowire experiments [16]. By exploring the properties of our ladder model, we provide further intuition about the structure of such 2D chiral phases.

The structure of this paper is as follows. In Sec. II we first introduce the details of the model Hamiltonian for the chiral ladder with three-spin interactions. Then, we explain briefly the expected behavior from Kadanoff coarse graining and small-size exact diagonalization results, before we discuss its bosonization. In Sec. III we explain some details about the implementation of our numerical method, namely, SU(2)-invariant iDMRG. In Sec. IV we present the results of our simulation, where we show that the ground state of the system corresponds to a conformal field theory (CFT) with $c = 1$. We additionally study the algebraic decay of spin-spin and dimer-dimer correlation functions, as well as the entanglement spectrum and the convergence of the ground-state energy. Our results for the entanglement spectrum are remarkably similar to those of the spin-$\frac{1}{2}$ Heisenberg chain, which we take as a strong indication that the CFT at low energies is a SU(2)$_1$ WZW theory. We wrap up our conclusions in Sec. V. Finally, in the Appendices we compute the spin-current operators (Appendix A), review the continuum limit of the model by Huang *et al.* presented in Ref. [11] (Appendix B), and explain the details of how to construct the SU(2)-invariant MPO for the Hamiltonian that we want to simulate (Appendix C), focusing on chiral three-spin interactions. In Appendix D we provide numerical data on the finite-entanglement scaling of the entanglement spectrum.

II. CHIRAL LADDER

A. Model

The model that we analyze in this paper is a two-leg ladder with chiral interactions on triangles. Specifically, it is a model of spin-$\frac{1}{2}$ on the sites of the ladder of Fig. 1 via the three-spin interaction Hamiltonian

$$H = \sum_i J_i \mathbf{S}_i \cdot (\mathbf{S}_{i+1} \times \mathbf{S}_{i+2}), \qquad (1)$$

with $\mathbf{S}_i$ the spin-$\frac{1}{2}$ operator at site i. The sites of the ladder are labeled in a snakelike pattern as shown in the details of the ladder in Fig. 2 and both triangles follow this snakelike labeling (upper triangles 1-2-3, lower triangles 2-3-4). We

will consider the cases where $J_i \in \{\pm 1\}$ in which the coupling coefficients depend on the traversal of the triangle. A triangle formed by sites i, $i + 1$, $i + 2$ is traversed in (against) the direction of the labels if $J_i = 1$ ($J_i = -1$). This can be rephrased to clockwise or anticlockwise configurations for each triangle. The triangles of the full ladder are all clockwise configured if $J_i = (-1)^i$ [anticlockwise if $J_i = -(-1)^i$]. Mixing the two scenarios gives rise to $J_i = 1 \ \forall i$ ($J_i = -1 \ \forall i$), which leads to a staggered, anticlockwise/clockwise (clockwise/anticlockwise) configuration pattern.

Playing with different clockwise/anticlockwise configurations of the triangles, we can get different Hamiltonians. For instance, for a unit cell of two triangles we can get the four configurations presented in Fig. 2. In the figure, two of the configurations (H_1 and H_2) have the same orientation of the triangles (i.e., both clockwise or both anticlockwise), and two (H_3 and H_4) have opposite orientation (i.e., one clockwise and one anticlockwise). Since we have $H_1 = -H_2$ and $H_3 = -H_4$, both pairs of Hamiltonians have the same energy spectrum. Therefore, for the physical properties only the relative orientation between the two triangles matters and it is sufficient to restrict to H_1 and H_3 as different cases.

Both Hamiltonians are odd under time-reversal symmetry ($\mathbf{S}_i \rightarrow -\mathbf{S}_i$), which results in $\mathcal{T}H_i\mathcal{T}^{-1} = -H_i$. The combination of two mirror symmetries (which is equivalent to an inversion at the chain center) leaves Hamiltonian H_1 invariant, whereas H_3 transforms as $\mathcal{P}H_3\mathcal{P}^{-1} = -H_3$. This main difference between the two cases with different relative triangle orientations (H_1 and H_3) results in different behavior of the

edge states: while edge states for H_1 are expected to be counterpropagating, they propagate in the same direction for H_3 (see the arrows in Fig. 2). In what follows, we show that this intuition is indeed true.

B. First intuition with Kadanoff coarse graining

The first approach we take to understand the dominant physics of the model consists in a Kadanoff-type coarse-graining procedure of the triangles into effective spin-$\frac{1}{2}$'s. In particular, we simply (i) project the 2^3-dimensional Hilbert space of the triangle n starting at site $i = 3n - 2$ onto the two-dimensional subspace of lowest energy via the isometry $W_n : \frac{1}{2} \otimes \frac{1}{2} \otimes \frac{1}{2} \longrightarrow \frac{1}{2}$, (ii) construct the representation of the operators $W_n \mathbf{S}_j W_n^\dagger$ and $W_n (\mathbf{S}_j \times \mathbf{S}_{j+1}) W_n^\dagger$ in this subspace, and then (iii) look for the emerging Hamiltonian.

The first step is rather easy, once we recall that the SU(2)-invariant Hamiltonian triangle term of Eq. (1) has to be proportional to the identity in the different subspaces with definite total spin, that it has null trace, and that it will be vanishing once the three spins are all parallel arranged. Indeed, a bit of algebra with Pauli matrices and Levi-Civita symbols leads to the expression

$$\mathbf{S}_1 \cdot (\mathbf{S}_2 \times \mathbf{S}_3) = \sum_{\alpha = \pm} \alpha \frac{\sqrt{3}}{4} \mathbb{P}_{1/2, \alpha} + 0 \, \mathbb{P}_{3/2}, \qquad (2)$$

where $\frac{1}{2} \otimes \frac{1}{2} \otimes \frac{1}{2} = \frac{1}{2}_+ \oplus \frac{1}{2}_- \oplus \frac{3}{2}$ and $\mathbb{P}$ are the corresponding projectors. $\frac{1}{2}_\pm$ are the subspaces of the spin-$\frac{1}{2}$ states with positive and negative energy. The searched isometry will then be depending on the sign of the triangle coupling, i.e.,

$$W_n W_n^\dagger = \mathbb{P}_{1/2, -\text{sgn}(J_{3n-2})}. \qquad (3)$$

Next, we have to construct the coarse-grained expressions of the spin operators involved in the interaction between triangles n and $n + 1$. It turns out that we can choose the projectors such that $\forall \, j \in \{3n - 2, 3n - 1, 3n\}$ and $\alpha \in \{\pm\}$,

$$W_{1/2, \alpha} \mathbf{S}_j W_{1/2, \alpha}^\dagger = \tfrac{1}{3} \widetilde{\mathbf{S}}_n, \qquad (4)$$

$$W_{1/2, \alpha} (\mathbf{S}_j \times \mathbf{S}_{j+1}) W_{1/2, \alpha}^\dagger = \frac{\alpha}{\sqrt{3}} \widetilde{\mathbf{S}}_n \qquad (5)$$

with $\widetilde{\mathbf{S}}_n$ the new effective spin-$\frac{1}{2}$. The resulting effective Hamiltonian then reads as

$$H_{\text{eff}} = -\text{sgn}(J_1 J_2) \frac{|J_1| + |J_2|}{3\sqrt{3}} \sum_{n=1}^{N} \widetilde{\mathbf{S}}_n \cdot \widetilde{\mathbf{S}}_{n+1}, \qquad (6)$$

where $N \simeq L/3$ is the total number of effective triangles, and we neglected an additive term $-\frac{\sqrt{3}}{4} \frac{|J_1| + |J_2|}{2} N$. We thus obtained an emerging spin-$\frac{1}{2}$ Heisenberg chain, whose magnetic character (ferromagnetic or antiferromagnetic) depends on the mutual signs of the triangle couplings J_1 and J_2, and we can resort to a wealth of known facts to foresee the behavior of our triangle ladder.

If the triangles are all (anti)clockwise oriented (H_1 and H_2), then the effective model (6) is antiferromagnetic: we therefore predict that it will be gapless, with central charge $c = 1$, and that its ground state would tend to minimize the total spin of the chain, i.e., for even N will be in the zero total

spin sector. Conversely, if the triangles have mixed character (H_3 and H_4), then the effective model (6) is ferromagnetic: we have thus good reasons to expect that the system will try to maximize its total spin, giving rise to a macroscopic degeneracy of the ground-state manifold, and without a well-defined CFT character. Of course, such low-energy projection is a very strong simplification and further corrections would be needed to describe the full richness of the model (e.g., the degeneracy counting of the case $J_1 = J_2$ in finite systems will be nontrivial). But, still, we will see below that the main results obtained by this simple analysis are in fact confirmed by more sophisticated theoretical and numerical approaches.

C. Exact diagonalization of small systems

The intuition obtained from the Kadanoff blocking in the previous section can be further corroborated by a simple exact diagonalization exercise. Specifically, here we perform exact diagonalization for small sizes, in particular for 16 spins. For this case, we compute the ground state and low-energy excited states and evaluate some observables. Of particular interest in order to assess chirality are spin-current operators of the form

$$\mathcal{J}_{i,i+1}^z = -J_{i-1} S_{i-1}^z (\mathbf{S}_i \mathbf{S}_{i+1}) - J_i (\mathbf{S}_i \mathbf{S}_{i+1}) S_{i+2}^z,$$

$$\mathcal{J}_{i,i+2}^z = -J_i (\mathbf{S}_i \mathbf{S}_{i+2}) S_{i+1}^z, \qquad (7)$$

which describe the flow of the z component of magnetization from site i to sites $i + 1$ and $i + 2$, respectively [notice that, by SU(2) invariance, there is not a preferred spin-component]. $\mathcal{J}_{i,i+1}^z$ measures the currents on the rung and slash links, to which there are contributions from two triangles. $\mathcal{J}_{i,i+2}^z$ measures the currents in the chains with only a single triangle contribution. The current operators can be derived by taking the commutator of the spin operator and the Hamiltonian, which is presented in Appendix A for a general N-leg ladder. For the wave functions obtained from our small-size exact diagonalization, we evaluate the expectation value of this current operator for the *up, down, rung,* and *slash* pairs of sites. Notice that in the chosen basis described below there are no $\mathcal{J}^x$ and $\mathcal{J}^y$ current components, so that the plotted current $\mathcal{J}^z$ is the total current in the system.

For the Hamiltonian configuration H_1 (or equivalently H_2), we find from our results that the ground state is a singlet of SU(2) with total spin zero, i.e., $\langle \mathbf{S}^2 \rangle = 0$ with $\mathbf{S}$ the total spin vector operator. Thus, we find that the ground state does not carry any currents. However, in the first excited state [an SU(2) triplet] the pattern of currents for every pair of sites corresponds to the one in Fig. 3, where we show both open and periodic boundary conditions. The chirality of the currents in the bulk is clear, and matches the intuition from Fig. 2.

Complementarily, for the Hamiltonian configuration H_3 (or equivalently H_4), we find that the ground state has a well-defined total spin and is also degenerate, according to the data in Table I. In this case, we diagonalize the subspace of degenerate ground states in the $\mathbf{S}^2$ and the S^z bases and pick states with fixed total and z component of the spin. We find that in such ground states there is a nontrivial current behavior, as shown in Fig. 4. Again, the observed pattern also matches our intuitive picture from Fig. 2.
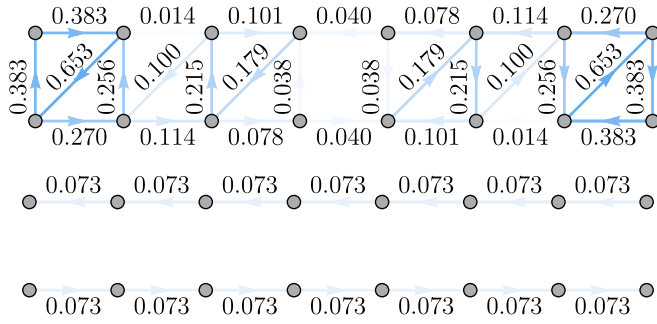
FIG. 3. Expectation values of the link currents for the first excited state of H_1 with 16 spins and $\langle \mathbf{S}^2 \rangle = 2$, $S^z = -1$ for open boundary conditions (top) and periodic boundary conditions (bottom). The color refers to the strength of the currents normalized to the maximal current $\mathcal{J}^{\max} = 0.107$ in Figs. 3 and 4. Both cases have counterpropagating edge currents, with periodic boundary conditions showing translation invariance and no currents on the rung and slash links. The first excited state with $\langle \mathbf{S}^2 \rangle = 2$ and $S^z = 0$ does not show $\mathcal{J}^z$ current expectation values, for $S^z = +1$ the current patterns are inverted.
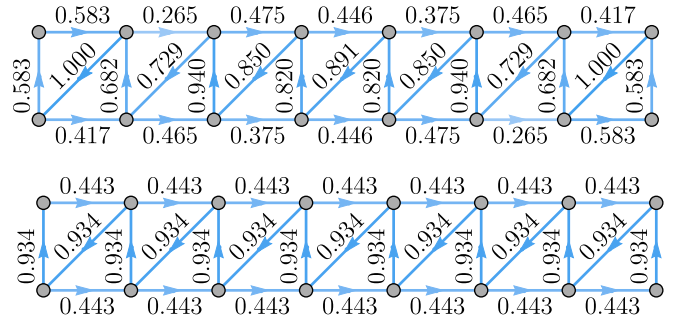

FIG. 4. Expectation values of the link currents for the ground state of H_3 with 16 spins and $\langle \mathbf{S}^2 \rangle = 12$, $S^z = -3$ for open boundary conditions (top) and periodic boundary conditions (bottom). The color refers to the strength of the currents normalized to the maximal current $\mathcal{J}^{\max} = 0.107$ in Figs. 3 and 4. Both cases have copropagating edge currents, with periodic boundary conditions showing translation invariance and no oscillations in the strength of the currents. The ground state with $\langle \mathbf{S}^2 \rangle = 12$ and $S^z = 0$ does not show $\mathcal{J}^z$ current expectation values, for $S^z = +3$ the current patterns are inverted.

From our small-size study with exact diagonalization we learn a couple of important things in order to study this model. First, configurations H_3 and H_4 do *not* have counterpropagating chiral edge modes and, moreover, have a *covariant* ground state with a well-defined, nonzero, total spin S; therefore, the ground manifold is a $(2S + 1)$-plet. Second, configurations H_1 and H_2 have counterpropagating chiral edge modes as well as a singlet ground state, which is thus SU(2) invariant.

As a matter of fact, the reason for the ground state of H_3 breaking SU(2) symmetry down to U(1) lies in the different overall character of the Hamiltonian: as readily visible on short chains, H_1 is globally antiferromagnetic, while H_3 is instead ferromagnetic. This means, practically, that the ground state of H_1 belongs to the singlet sector (total spin zero), while the energy for H_3 would be minimized by a state with large spin. If we do not make use of symmetries, the multiplicity of the H_3 ground-state manifold diverges at the targeted thermodynamic limit, thus making it difficult for numerical algorithms to converge.

TABLE I. Ground-state degeneracy and total spin for different lengths, for configurations H_3 and H_4.

No. Spins	Degeneracy	Total spin
4	3	1
6	3	1
8	5	2
10	5	2
12	7	3
14	7	3
16	7	3
18	9	4
20	9	4
22	11	5
24	11	5

Given the above, in this paper we choose to analyze in detail the ground state of configuration H_1 (or equivalently H_2), which is an SU(2) singlet, with an SU(2)-invariant infinite DMRG code. The case of configuration H_3 (and H_4) could be better assessed by an MPS code that incorporates U(1) symmetry instead, and/or an SU(2) code that can target generic covariant states. Therefore, we focus here entirely on the configuration providing an SU(2)-invariant ground state.

D. Bosonization

A wide class of interactions can be treated by Jordan-Wigner transformation followed by bosonization of the fermionic modes [17,18]. We start with the following set of definitions:

$$S_j^+ = e^{+i\phi_j} c_j^\dagger, \quad S_j^- = e^{-i\phi_j} c_j, \quad S_j^z = n_j - 1/2, \quad (8)$$

where $\phi_j = \pi \sum_{k<j} S_k^+ S_k^-$ is the Jordan-Wigner string. A term $h(j) = J_j \mathbf{S}_j \cdot (\mathbf{S}_{j+1} \times \mathbf{S}_{j+2})$ of three consecutive spins with coupling J_j will transform to $h(j) \to J_j[T(j) + V(j)]$. The kinetic and interacting terms read as

$$T(j) = -\frac{i}{4}(c_j^\dagger c_{j+1} - c_j^\dagger c_{j+2} + c_{j+1}^\dagger c_{j+2}) + \text{H.c.},$$

$$(9)$$

$$V(j) = +\frac{i}{2}(c_j^\dagger c_{j+1} n_{j+2} + n_j c_{j+1}^\dagger c_{j+2}) + \text{H.c.},$$

with density operator $n_j = c_j^\dagger c_j^\dagger$. The full kinetic part of the two-site invariant Hamiltonian in Eq. (1) reads as

$$H_{\text{kin}} = \sum_{j \text{ odd}} J_1 T(j) + J_2 T(j+1), \quad (10)$$

which is simply a tight-binding model of spinless fermions on a triangular lattice with nonzero fluxes for generic couplings J_1 and J_2. For the case $J_1 = -J_2$, two parts of the tight-binding Hamiltonian become fully disconnected. To see this, we use a two-site unit cell according to the drawings in the introductory chapter with sublattices A (upper chain) and B (lower chain)
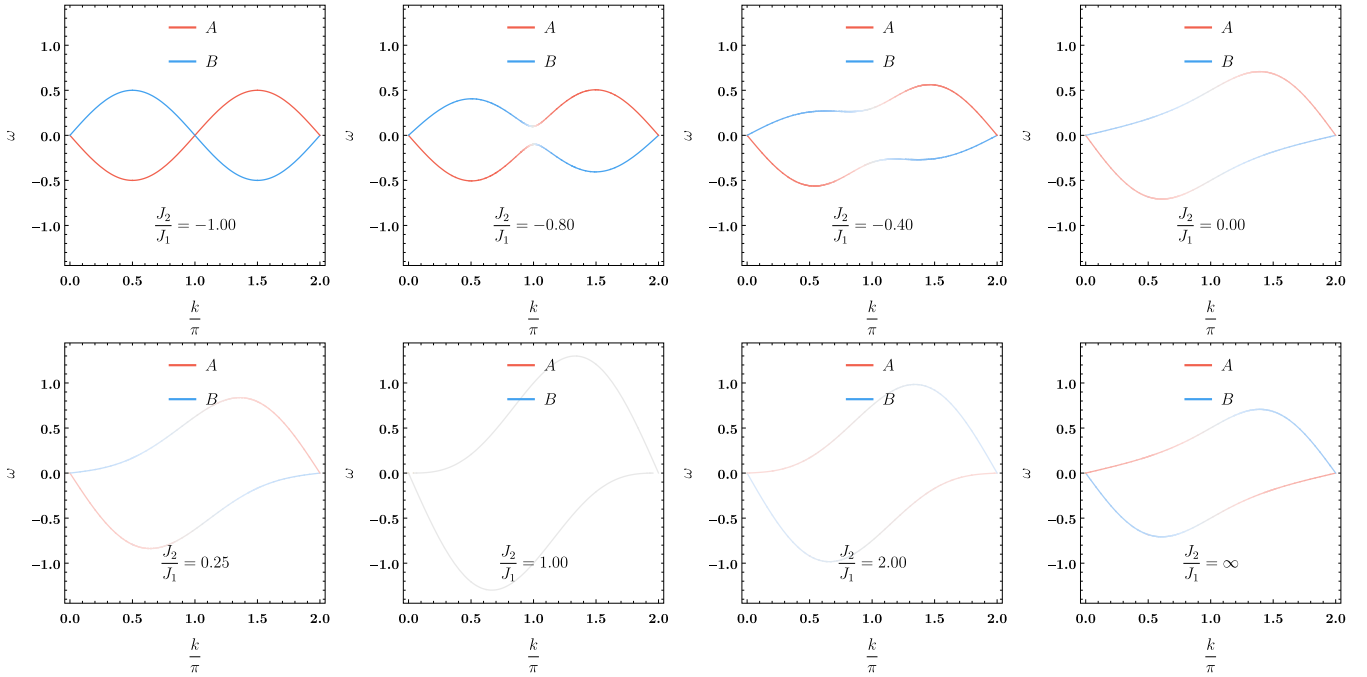
FIG. 5. Dispersion for different coupling strengths. The color indicates the polarization of the bands. In the case we study in the paper, both bands are fully polarized and the kinetic dispersion is $\omega(k) = \pm\frac{1}{2}\sin(k)$. If we tune $\frac{J_2}{J_1} > -1$, we allow for a mixing between A and B, and only one of the avoided crossings is preserved.

and a spinor $d_k = (c_{A,k}\ c_{B,k})^\top$. The tight-binding Hamiltonian in this basis and after a subsequent Fourier transformation reads as $H_{\mathrm{kin}} = \sum_k d_k^\dagger h(k) d_k$ and reduces to a sum of 2×2 matrices given by

$$h(k) = -\frac{1}{4}\begin{pmatrix} 2J_1 \sin k & iJ_+(1 - e^{-ik}) \\ -iJ_+(1 - e^{+ik}) & 2J_2 \sin k \end{pmatrix}, \quad (11)$$

where $J_+ = J_1 + J_2$. Without further restrictions, we assume $J_1 \geqslant 0$ to avoid unnecessary ambiguities in the ordering of the bands and show the resulting dispersion in Fig. 5. If we consider $J_1 = +1$ and $J_2 = -1$ (i.e., H_1), we see two cosine bands which are shifted by $\pm\frac{\pi}{2}$ according to the nonzero flux threading the two sublattices. The two Fermi points correspond to a central charge of $c = 2$. If we slightly increase J_2, we find $H(k = 0) = 0$, that is, there are no scattering

processes and the dispersion (i.e., the band crossing) will be left untouched. However, at momentum $k = \pi$, there are strong interchain transitions, i.e., $H(k = \pi) = \frac{1}{2}(J_1 + J_2)\sigma_y$ which yields the observed avoided crossing.
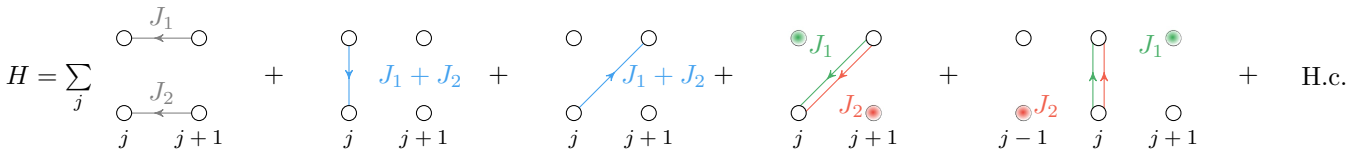
The interacting part of the Hamiltonian reads as

$$H_{\mathrm{int}} = \sum_{j\ \mathrm{odd}} J_1 V(j) + J_2 V(j + 1), \quad (12)$$

which can again be written in terms of the two-site basis

$$H_{\mathrm{int}} = \frac{i}{2}\sum_j [(J_1 n_{j+1,A} + J_2 n_{j-1,B})c_{j,A}^\dagger c_{j,B}$$
$$+ (J_1 n_{j,A} + J_2 n_{j+1,B})c_{j,B}^\dagger c_{j+1,A}] + \mathrm{H.c.} \quad (13)$$

For better understanding, we visualize all hopping terms of the full Hamiltonian

Here, the colored sites (filled circles) correspond to the density and the arrows indicate a hopping operator. It is now apparent that the interactions enable the same interchain tunnelings as the single-particle ones (up to a phase and additional density dependencies). Albeit the isolated study of chiral interactions in existing materials is quite unrealistic, we showed here that it is equivalent to a simple fermionic tight-binding

model combined with density-assisted hoppings in a quasi-one-dimensional ladder setup. A combination of such terms was proposed for experiments in the framework of ultracold atoms trapped in optical lattices [19] and has been realized very recently [20].

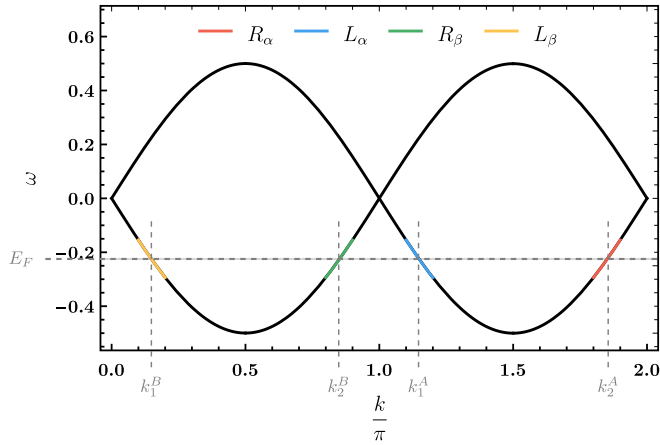In order to understand the gapping mechanism in the model, we start from Hamiltonian H_1 ($J_1 = -J_2 = +1$) with

FIG. 6. At the Fermi energy E_F the linearized spectrum consists of left- and right-moving species for each flavor A, B.

two identical bands which are displaced by a phase π in momentum space. If we fix the density at a Fermi energy E_F such that the Fermi momentum k_F is in the vicinity of the linear regime of the dispersion, we are allowed to linearize the spectrum. The linearization of such a dispersion is fairly standard and can be described by a Luttinger liquid (LL)

$$
H_{\text{LL}} = v_F \sum_{\alpha \in \{A,B\}} \sum_k \left(R_\alpha^\dagger(k)\left(k - k_2^\alpha\right)R_\alpha(k) \right.
$$
$$
\left. - L_\alpha^\dagger(k)\left(k + k_1^\alpha\right)L_\alpha(k) \right), \tag{14}
$$

where $R/L_\alpha(k)$ denote right- and left-moving modes of the linearized dispersion in the vicinity of the Fermi momenta k_i^α and $v_F = \frac{1}{2}\cos(k_2^\alpha)$ is the Fermi velocity (see Fig. 6).

We now proceed by rewriting the fermionic modes in terms of right- and left-moving fields $R/L_\alpha(x)$:

$$
c_A(x) \propto e^{ik_1^A x}L_A(x) + e^{ik_2^A x}R_A(x),
$$
$$
c_B(x) \propto e^{ik_1^B x}L_B(x) + e^{ik_2^B x}R_B(x). \tag{15}
$$

The local densities for both species $\alpha \in \{A, B\}$ can be expressed in terms of the new modes

$$
n_\alpha(x) \propto n_{\alpha,R}(x) + n_{\alpha,L}(x) + \left(e^{i(k_1^\alpha - k_2^\alpha)x}R_\alpha^\dagger(x)L_\alpha(x) + \text{H.c.} \right). \tag{16}
$$

The gap opening in Fig. 5 can be explained by a perturbative expansion in J_+. Going back to the general noninteracting Hamiltonian, the A, B scattering processes become

$$
J_+\Delta h(x) \propto \frac{J_+}{2i}[c_A^\dagger c_B - c_A^\dagger(x+a)c_B] + \text{H.c.}
$$
$$
\approx \frac{J_+}{2i}[2R_A^\dagger(x)L_B + (\partial_x L_A^\dagger(x))R_B] + \text{H.c.} \tag{17}
$$

The first term ($\propto R_A^\dagger L_B$) is a relevant, the other an irrelevant, perturbation to the Luttinger liquid Hamiltonian.

Among many other (supposedly irrelevant) terms of the interacting Hamiltonian in Eq. (13), which we do not devote our main focus to, we obtain a marginal term

$$
H_{\text{int}} \approx -2\sum_j n_{AB}(j)\Delta h(j). \tag{18}
$$

This yields up to a sign the same scattering process between the sublattices as encountered in Eq. (17), only here it is multiplied by the density

$$
n_{AB}(j) = J_1[n_{A,L}(j) + n_{A,R}(j)] + J_2[n_{B,L}(j) + n_{B,R}(j)]. \tag{19}
$$

The simple Abelian bosonization approach presented in this section is already sufficient to explain two important features. First, by coupling right movers of sublattice A with left movers of sublattice B, a gap opens up around $k = \pi$. This removes one of the two Fermi points and the interaction drives the system from a central charge $c = 2$ to $c = 1$ in a similar fashion as the noninteracting term. Furthermore, it explains the chiral current propagation of the low-lying energy excitations observed in the exact diagonalization (see Fig. 3). To predict the long-distance behavior of correlation functions, we resort instead to more sophisticated non-Abelian bosonization techniques. In Appendix B, we recap the continuum limit of the model by Huang and coauthors following Ref. [11] and present the expected analytic behavior for spin-spin correlations.

III. METHODS

The numerical method that we used to compute the ground-state properties of the model is infinite DMRG [6]. The iDMRG algorithm has been extensively discussed many times in the literature (see, e.g., Sec. III of Ref. [21]). In our specific implementation we used the two-site update for an infinite MPS with a two-site unit cell. Each physical index of the MPS has dimension 4, and describes the upper and lower spin-$\frac{1}{2}$ of each rung of the ladder. Moreover, we implemented SU(2) symmetry using the scheme that we described in Ref. [9], based on the formalism of fusion trees to target the SU(2)-symmetric ground state of the ladder configuration $J_1 = -J_2 = -1$ (H_1). Therefore, the physical index of the MPS carries the quantum numbers $\frac{1}{2} \otimes \frac{1}{2} = 0 \oplus 1$.

Apart from the implementation of SU(2) symmetry, our iDMRG method heavily relies on the correct implementation of the MPO for the Hamiltonian with SU(2) symmetry. While the case of three-spin interactions is implicitly discussed in the literature, a more in-depth discussion of this case would be particularly useful. We describe the details of how to implement such an MPO in Appendix C.

TABLE II. Symmetric and effective bond dimensions for several simulations together with the irreps and degeneracies on the virtual bonds of the MPS.

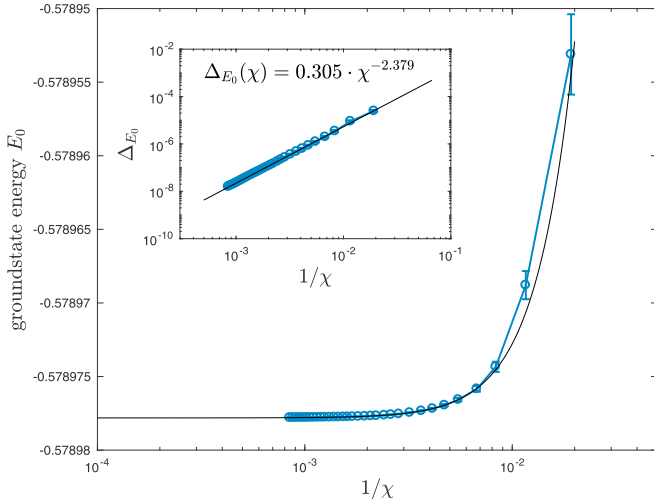| χ_{sym}	χ	Virtual bond irreps
50	148	$0_{14} \oplus 1_{24} \oplus 2_{11} \oplus 3_1$
100	312	$0_{26} \oplus 1_{46} \oplus 2_{24} \oplus 3_1$
150	480	$0_{37} \oplus 1_{68} \oplus 2_{38} \oplus 3_7$
200	652	$0_{48} \oplus 1_{89} \oplus 2_{52} \oplus 3_{11}$
250	834	$0_{58} \oplus 1_{110} \oplus 2_{65} \oplus 3_{16} \oplus 4_1$
300	1008	$0_{69} \oplus 1_{130} \oplus 2_{80} \oplus 3_{20} \oplus 4_1$
350	1184	$0_{80} \oplus 1_{149} \oplus 2_{96} \oplus 3_{24} \oplus 4_1$

FIG. 7. Convergence of the ground-state energy E_0 with the MPS bond dimension χ. Here, we use the discarded weight (see also Fig. 8) as an estimate of the relative error for the ground-state energy in each simulation. The inset shows the convergence of the error $\Delta_{E_0} = E_0 - E_0(\chi \to \infty)$ between the energy and its extrapolated value.

IV. RESULTS

A. Energy convergence

Let us start by showing the results for the energy convergence of our SU(2) iDMRG code for the considered chiral Hamiltonian on a ladder. In order to give an overview of simulation parameters and the corresponding irreps on the virtual bonds, we listed some examples in Table II. The convergence of the energy with the effective MPS bond dimension χ is shown in Fig. 7, where we use up to $\chi \approx 1200$. In the aforementioned figure, convergence is only approached for very large bond dimension $\chi \gtrsim 1000$, which would be difficult to reach without SU(2)-symmetric tensors. In Fig. 8
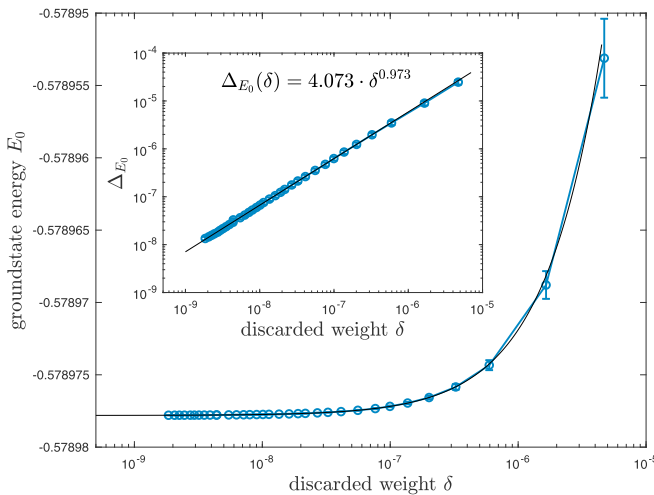
FIG. 8. Convergence of the ground-state energy E_0 with the iDMRG discarded weight. The inset shows the convergence of the error $\Delta_{E_0} = E_0 - E_0(\chi \to \infty)$ between the energy and its extrapolated value.
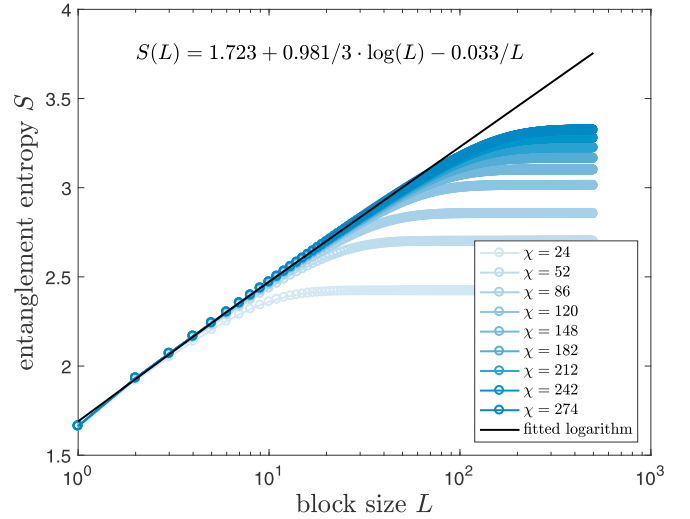
FIG. 9. Scaling of the entanglement entropy $S(L)$ for a block of size L and different bond dimensions χ. Computing the entanglement entropy of a block is restricted to only moderate bond dimensions due to a higher computational cost of $O(\chi^5)$ compared to the semi-infinite chain which scales like $O(\chi^3)$.

we show a similar plot, namely, the convergence of the ground-state energy with the discarded weight in the iDMRG approximation. As is well known, this allows for a better extrapolation to the $\chi \to \infty$ limit [22]. In our case, we obtain an estimate of

$$E_0(\chi \to \infty) \approx -0.578\,978(2). \tag{20}$$

In the insets of Figs. 7 and 8 we plot the convergence of the error $\Delta_{E_0} = E_0 - E_0(\chi \to \infty)$ between the energy and its extrapolated value, as a function of the inverse effective MPS bond dimension $1/\chi$ and the discarded weight, respectively.[2]

B. Entanglement

We studied several entanglement figures of merit in our system. First, in Fig. 9 we show the scaling of the entanglement entropy $S(L)$ of a block of length L with two open ends, for different values of the bond dimension χ. The computational cost of this calculation is $O(\chi^5)$, as opposed to the $O(\chi^3)$ cost of infinite DMRG. Thus, we are restricted to only moderate values of the bond dimension for the calculation of the entanglement entropy. Before reaching saturation due to finite χ for large block sizes, the data follow a CFT scaling $S(L) \sim c/3 \log L$ [24]. In our case, this implies that $c \approx 1$, as seen in the plot, where we also show our best fit including $O(1/L)$ subleading corrections. Furthermore, we also analyzed the scaling of the entanglement entropy of half an infinite chain with the MPS correlation length ξ, a calculation that instead scales like $O(\chi^3)$. The result shown

---

[2]Generally, the convergence of the ground-state energy with respect to the discarded weight should be fitted with a linear function [23]. This, however, is in good agreement with our power-law fit that shows an exponent of 0.973.
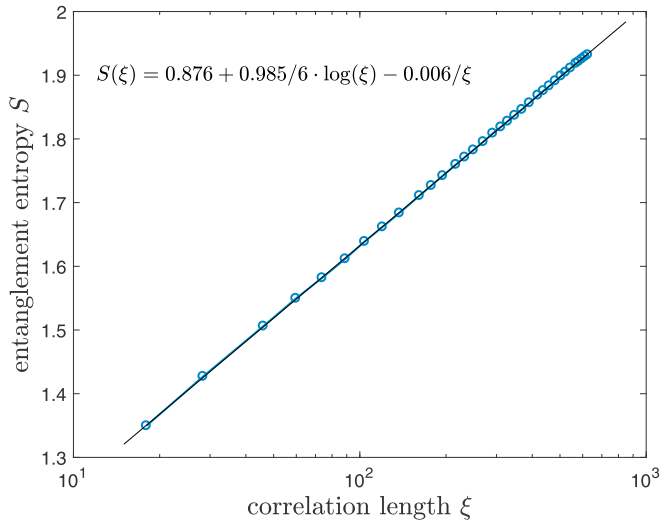
FIG. 10. Scaling of the entanglement entropy $S(\xi)$ for half an infinite chain with the MPS correlation length ξ for up $\chi = 1184$.

in Fig. 10 matches perfectly a CFT scaling $S(\xi) \sim c/6 \log \xi$, again with central charge $c \approx 1$.

In order to assess the consistency of our calculations, we computed the finite-entanglement scaling of the MPS correlation length ξ with the bond dimension χ [7]. In Fig. 11 we see that this follows a perfect algebraic fit $\xi \sim \chi^\kappa$, with exponent $\kappa \approx 1.16$, which following the *approximate* formula $\kappa \approx 6/[c(\sqrt{12/c} + 1)]$ [7], is again compatible with $c \approx 1$.

C. Correlation functions

In order to assess the criticality of the system, we computed a number of SU(2)-invariant correlation functions $C(r = |i - j|)$ in the system, with positions i, j and relative distance r (notice that the sites i, j can belong to different ladder legs). We observed algebraic decays and critical exponents, following $C(r) \sim r^{-\alpha}$. We computed all correlation
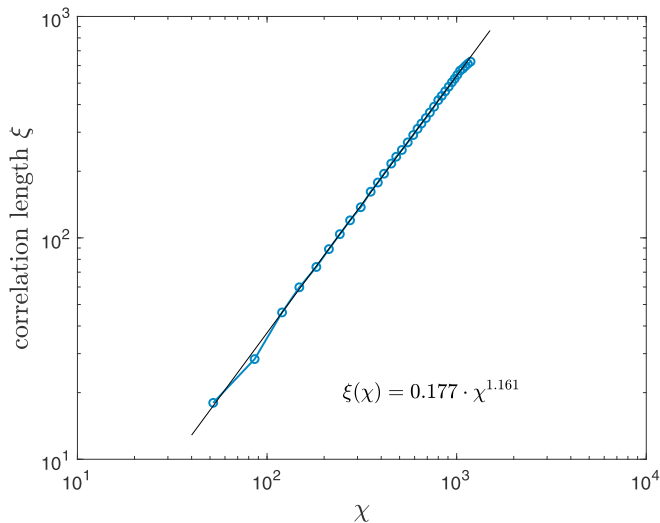
FIG. 11. Scaling of the MPS correlation length ξ with the bond dimension χ.
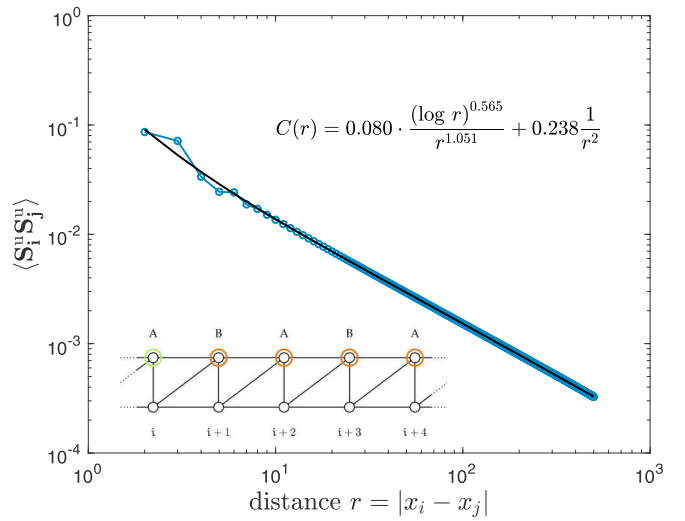

FIG. 12. Spin-spin correlation function between spins in the same chain. The two-point correlation function is expected to follow $C(r) \sim (\log r)^{1/2}/r$, which is in good agreement with the numerical data [25,26]. The exponent for the short-distance term is fixed.

functions for an MPS with bond dimension $\chi = 1184$ ($\chi_{\rm sym} = 350$).

1. Spin-spin correlator

First, we computed the spin-spin correlation functions $\langle \mathbf{S}_i^u \mathbf{S}_j^u \rangle$ and $\langle \mathbf{S}_i^u \mathbf{S}_j^d \rangle$, where i, j are the rung indices and u, d the leg indices, respectively. As shown in Figs. 12 and 13, we observe a similar algebraic decay in both cases with exponent $\alpha \approx 1$. This indeed matches the expectation from the continuum limit calculation in Eq. (B12). Additional logarithmic corrections for large distances are conform with the analytic prediction [25,26].
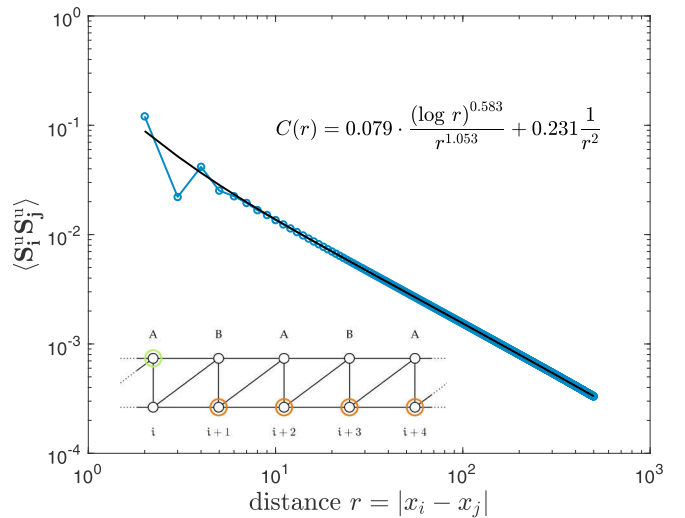

FIG. 13. Spin-spin correlation function between spins in different chains. The two-point correlation function is expected to follow $C(r) \sim (\log r)^{1/2}/r$, which is in good agreement with the numerical data [25,26]. The exponent for the short-distance term is fixed.
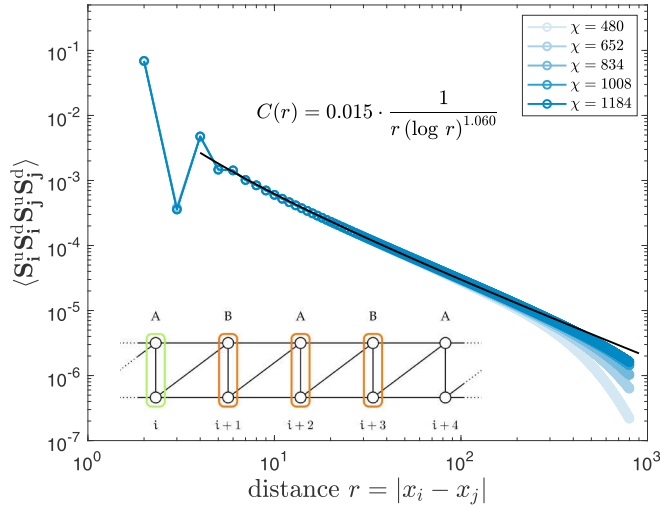
FIG. 14. Dimer-dimer correlation function between vertical dimers with logarithmic corrections. The correlations for smaller bond dimensions show an exponential tail due to the final amount of entanglement in the MPS. For larger bond dimension, the correlation is expected to follow the fitted function to even larger separation distances.

2. Dimer-dimer correlator

Next, we studied the dimer-dimer correlation function between vertical dimers $\langle (\mathbf{S}_i^u \mathbf{S}_i^d)(\mathbf{S}_j^u \mathbf{S}_j^d) \rangle$. The four-body correlation is corrected by all possible disconnected parts, namely, $\langle \mathbf{S}_i^u \mathbf{S}_i^d \rangle \langle \mathbf{S}_j^u \mathbf{S}_j^d \rangle$, $\langle \mathbf{S}_i^u \mathbf{S}_j^u \rangle \langle \mathbf{S}_i^d \mathbf{S}_j^d \rangle$, and $\langle \mathbf{S}_i^u \mathbf{S}_j^d \rangle \langle \mathbf{S}_i^d \mathbf{S}_j^u \rangle$ with appropriate factors. The result is shown in Fig. 14, where the decay fits very well an algebraic decay, as expected for criticality, with decay exponent $\alpha \approx \frac{5}{4}$.

D. Entanglement spectrum

In order to further characterize the model, we also studied the entanglement spectrum of half an infinite chain. The singular values are readily available and their distribution is according to the virtual bond irreps shown in Table II, where each spin sector S comes with a $2S + 1$ degeneracy. Notice that, by construction, S will always be an integer because of the coarse graining of the two spin-$\frac{1}{2}$'s from the upper and lower legs to form the MPS.

In Fig. 15 we show our results for the entanglement energies $\varepsilon_\alpha \equiv -\log \lambda_\alpha^2$ with λ_α the Schmidt coefficients of half an infinite chain. The results are organized according to the different spin sectors $S = 0, 1, 2, 3,$ and 4 of the bond dimension [so that each point in the plot is indeed a $(2S + 1)$-plet]. Results for our ladder model with triangles (TM) are given by the squares. In addition, we compare the results of the chiral ladder to the values of ε_α that we obtain when computing the ground state of the spin-$\frac{1}{2}$ Heisenberg spin chain (HM) with the same numerical method, and after coarse graining two sites into one (so that the MPS bond dimension also has integer spin sectors S). As can be seen in the plot, both spectra show exactly the same features up to an overall rescaling. This is especially true for the lowest part of the entanglement spectrum, i.e., the largest singular values, which are also most accurate. This is an important observation because it means
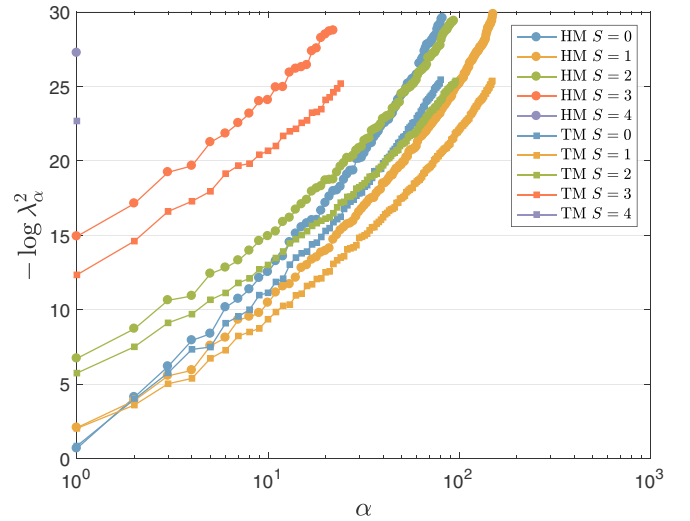

FIG. 15. Entanglement spectrum for the triangle ladder model (TM, squares) and the Heisenberg spin chain (HM, dots), with multiplets organized according to their spin sector S. Every point is a $(2S + 1)$-plet.

that the low-energy limits of both lattice systems (TM and HM) have quite probably the same boundary CFT [27], and in practice it means that both limits are probably described by the same $(1 + 1)$-dimensional CFT. Accordingly, this is a strong indication that the CFT for our chiral ladder model is likely the same than for the Heisenberg spin-$\frac{1}{2}$ chain, i.e., an $SU(2)_1$ WZW theory, which indeed would be in agreement with all our previous results as well as with the $SU(2)$ symmetry of the lattice model. Notice, though, that the continuum Hamiltonian in Eq. (B10) is not yet the one of an $SU(2)_1$ effective theory since it is written in terms of current operators for each leg of the ladder. For completeness, we also show the convergence of the entanglement spectrum with the MPS bond dimension in Appendix D.

V. CONCLUSIONS

In this paper we have studied a chiral two-leg ladder with $SU(2)$ symmetry using an $SU(2)$-invariant iDMRG algorithm. After getting some intuition about the model by Kadanoff coarse graining, exact diagonalization, and bosonization, we find numerically that the ground state of the system agrees with a CFT with central charge $c \approx 1$, which is also compatible with previous studies of the continuum limit. In particular, we analyzed the scaling of the entanglement entropy of a block and of half an infinite system, as well as finite-entanglement scaling, ground-state energy convergence, entanglement spectrum, and different correlation functions showing algebraic decay at long separation distances. Our results for the entanglement spectrum are compatible with an $SU(2)_1$ WZW theory in the low-energy limit. Moreover, we explained in full detail how to obtain $SU(2)$-invariant MPOs for three-spin interactions, something that so far had not been discussed in detail in the literature. Our procedure for constructing such MPOs can be generalized to arbitrary $SU(2)$-invariant interactions on 1D and quasi-1D systems.

Our work motivates further investigations along a number of directions. For instance, it would be interesting to dig deeper into the continuum limit of the model. The case of multileg and higher-spin ladders could also be analyzed with techniques similar to the ones in this paper. This would be particularly interesting in order to understand how two-dimensional physics emerges, and how the gapped/gapless nature of the *chiral* system depends on both the spin and the number of legs. An investigation of configuration H_3 with U(1)-invariant and/or SU(2)-covariant MPS methods would also be relevant in order to understand the overall physics of the chiral ladder configurations that we did not consider here. Investigating similar chiral Hamiltonians in kagome stripes would also be within reach and could lead to interesting physical insights. Finally, we expect that the simulations in this paper will help us to understand the procedure to simulate chiral quantum spin models in two spatial dimensions with SU(2)-invariant tensor networks such as projected entangled pair states (PEPS) [28–30].

ACKNOWLEDGMENTS

APPENDIX A: DERIVATION OF THE CURRENT OPERATOR

The operators to measure the spin currents flowing in the links of the ladder can be derived from the Hamiltonian

$$H = J_j \epsilon_{\alpha\beta\gamma} S_j^\alpha S_{j+1}^\beta S_{j+2}^\gamma \tag{A1}$$

using the Heisenberg equation of motion. Kirchhoff's law is satisfied for all the nodes in the lattice, and we can compute the spin currents passing each node according to

$$-\frac{\partial S_i^\mu}{\partial t} = -i[S_i^\mu, H] = -iJ_j \epsilon_{\alpha\beta\gamma}[S_i^\mu, S_j^\alpha S_{j+1}^\beta S_{j+2}^\gamma]$$
$$= J_i(S_i S_{i+1} S_{i+2}^\mu - S_i S_{i+2} S_{i+1}^\mu)$$
$$+ J_{i-1}(S_i S_{i+1} S_{i-1}^\mu - S_{i-1} S_i S_{i+1}^\mu)$$
$$+ J_{i-2}(S_{i-2} S_i S_{i-1}^\mu - S_{i-1} S_i S_{i-2}^\mu). \tag{A2}$$

For a general ladder with N chains, there are two currents on every link, one for each triangle the link appears in. The resulting 12 different currents per lattice site can be presented in a more intuitive way in Fig. 16. For the $N = 2$ leg ladder subject to analysis in the paper there are only six terms for every lattice site i, e.g., $\mathcal{J}_{i,n}$ with $n \in [1, 2, 3, 4, 5, 6]$ for the upper chain and $n \in [7, 8, 9, 10, 11, 12]$ for the lower chain assuming periodic boundary conditions. In case of open boundary conditions, one has to disregard nonexistent terms at the edges.

$$-\partial_t S_i = J_1 \left((S_i S_{i+1})S_{i+N} - (S_i S_{i+N})S_{i+1} \right)$$

$$+ J_2 \left((S_i S_{i+1})S_{i-N+1} - (S_i S_{i-N+1})S_{i+1} \right)$$

$$+ J_1 \left((S_i S_{i-N})S_{i-N+1} - (S_i S_{i-N+1})S_{i-N} \right)$$

$$+ J_1 \left((S_i S_{i+N-1})S_{i-1} - (S_i S_{i-1})S_{i+N-1} \right)$$

$$+ J_2 \left((S_i S_{i+N-1})S_{i+N} - (S_i S_{i+N})S_{i+N-1} \right)$$

$$+ J_2 \left((S_i S_{i-N})S_{i-1} - (S_i S_{i-1})S_{i-N} \right)$$

FIG. 16. All terms of the spin current operator contributing at each site of the ladder. We define incoming currents as being positive and outgoing currents as being negative. The current in each link of the ladder is a three-site observable which includes a scalar product (indicated by arrows) between two sites, and the multiplication with S on the third site (depicted as a blue colored circle).

APPENDIX B: CONTINUUM LIMIT

The ladder Hamiltonian in Eq. (1) has been considered in the literature in the presence of extra spin-spin Heisenberg-type interactions [11–13]. In these works, the low-energy continuum limit of our purely chiral lattice model H_1 (equivalently H_2) has also been computed (see, e.g., Appendix A of Ref. [11]). Here, we sketch briefly the main points of this derivation, and discuss some implications.

The key idea to derive the continuum limit is to use the same formalism as in Ref. [31] (see also Ref. [32]) to deal with the continuum limit of the antiferromagnetic Heisenberg quantum spin chain. Starting from a Hubbard-type Hamiltonian for fermions with spin (say, electrons), one considers operator $c_{i,\alpha}$ which annihilates an electron of spin α at site

i. Spin operators are then written in terms of these fermionic operators as

$$\mathbf{S}_i = \tfrac{1}{2} c_{i,\alpha}^\dagger \boldsymbol{\sigma}_{\alpha\beta} c_{i,\beta}, \tag{B1}$$

with $\boldsymbol{\sigma}$ a vector of Pauli matrices. As explained in Ref. [31], in the continuum limit the fermionic field is expanded around the Fermi points $k \approx \pm\pi/2$,

$$c_{i,\alpha} \rightarrow \psi_\alpha(x) \sim e^{-i\pi x/2}\psi_{L,\alpha}(x) + e^{i\pi x/2}\psi_{R,\alpha}(x), \tag{B2}$$

with $\psi_{L/R,\alpha}(x)$ slowly varying fields on the scale of lattice spacing a, which annihilate left–plx-sol-plxright-moving electrons. These chiral fermions can be bosonized as

$$\psi_{L/R,\alpha}(x) \sim e^{-i\sqrt{2\pi}\varphi_{L/R,\alpha}(x)}, \tag{B3}$$

with $\varphi_{L/R,\alpha}(x)$ chiral bosons. Introducing charge and spin degrees of freedom as

$$\varphi_{L/R,c}(x) = \frac{\varphi_{L/R,\uparrow}(x) + \varphi_{L/R,\downarrow}(x)}{\sqrt{2}},$$
$$\varphi_{L/R,s}(x) = \frac{\varphi_{L/R,\uparrow}(x) - \varphi_{L/R,\downarrow}(x)}{\sqrt{2}}, \tag{B4}$$

one can see that at half-filling (or, more restrictively, for one electron per lattice site), a small Hubbard interaction gaps out the charge mode. This can then be integrated out, and the low-energy properties are then described by spin physics. Moreover, for the Heisenberg model, the SU(2) spin symmetry is independently conserved for fields $\psi_{L/R,\alpha}(x)$ [31] which, following Noether's theorem, implies that one can write the conserved (chiral) currents

$$\mathbf{J}_{L/R} = \tfrac{1}{2} \psi_{L/R,\alpha}^\dagger \boldsymbol{\sigma}_{\alpha\beta} \psi_{L/R,\beta}. \tag{B5}$$

Thus, in the continuum limit, the lattice spin operators can be written as

$$a^{-1}\mathbf{S}_i \approx (\mathbf{J}_L + \mathbf{J}_R) + \tfrac{1}{2}(-1)^i(\psi_{L,\alpha}^\dagger \boldsymbol{\sigma}_{\alpha\beta} \psi_{R,\beta} + \text{H.c.}). \tag{B6}$$

Bosonizing the fermionic fields in the second term and integrating out the charge boson [31] one arrives at the expression

$$a^{-1}\mathbf{S}_i \approx (\mathbf{J}_L + \mathbf{J}_R) + (-1)^i \Theta \, \text{tr}(g_{\text{W}} \cdot \boldsymbol{\sigma}), \tag{B7}$$

with $g_{\text{W}}(x)$ the Wess-Zumino-Witten (WZW) field [i.e., an SU(2) matrix] and Θ a nonuniversal constant. Matrix $g_{\text{W}}(x)$ is explicitly given by

$$g_{\text{W}}(x) = \begin{pmatrix} e^{i\sqrt{2\pi}\varphi_s} & e^{i\sqrt{2\pi}\bar{\varphi}_s} \\ e^{-i\sqrt{2\pi}\bar{\varphi}_s} & e^{-i\sqrt{2\pi}\varphi_s} \end{pmatrix}, \tag{B8}$$

with $\varphi_s \equiv \varphi_{L,s} + \varphi_{R,s} \equiv (\varphi_{L,\uparrow} + \varphi_{R,\uparrow} - \varphi_{L,\downarrow} - \varphi_{R,\downarrow})/\sqrt{2}$ and $\bar{\varphi}_s \equiv \varphi_{L,s} - \varphi_{R,s} \equiv (\varphi_{L,\uparrow} - \varphi_{R,\uparrow} - \varphi_{L,\downarrow} + \varphi_{R,\downarrow})/\sqrt{2}$ following notation from Ref. [33]. Usually, one defines $\mathbf{n} \equiv \Theta \, \text{tr}(g_{\text{W}} \cdot \boldsymbol{\sigma})$, which physically amounts to a quantum field for the staggered magnetization. Thus, one finally arrives at the usual expression

$$a^{-1}\mathbf{S}_i \approx (\mathbf{J}_L + \mathbf{J}_R) + (-1)^i \mathbf{n}. \tag{B9}$$

This equation sets the connection between lattice spin operators and chiral spin-current fields. Thus, for a Hubbard-type system of electrons with exactly one electron per site, charge degrees of freedom are frozen and spin physics emerges entirely in terms of these operators. Importantly, for our

purposes, in Ref. [11] it was shown that with this substitution, the continuum limit of our chiral Hamiltonian H_1 is given by

$$H_1 \approx g \int dx (\mathbf{J}_{L,1} \cdot \mathbf{J}_{R,2} - \mathbf{J}_{R,1} \cdot \mathbf{J}_{L,2}), \tag{B10}$$

where $g = 4a/\pi$ with a the lattice spacing, and $\mathbf{J}_{L/R,1/2}$ is the chiral L/R current for the upper (1) or lower (2) legs of the ladder. Here, the approximation $\approx$ means that the equivalence holds up to irrelevant local perturbations, and in the limit of lattice spacing going to zero. The calculation arriving to this effective Hamiltonian, which we do not reproduce entirely here, makes use of operator product expansions and analyzes the existence of irrelevant terms in the continuum Hamiltonian. Notice that, as expected from the lattice Hamiltonian, the obtained quantum field theory is odd with respect to time-reversal symmetry (i.e., the exchange $L \leftrightarrow R$). As a remark, let us also mention that, recently, it has been shown that Eq. (B10) can also be written in terms of four Majorana fields for each leg [34].

In the CFT language, operators $\mathbf{J}_{L/R}$ are $\text{SU}(2)_1$ Kac-Moody chiral currents, and are the ones entering the $\text{SU}(2)_1$ WZW model as low-energy effective field theory of the spin-$\tfrac{1}{2}$ Heisenberg quantum spin chain [31]. Importantly, for our purposes, in Ref. [13] it was shown that the quantum field theory in Eq. (B10) for the chiral spin ladder is an RG fixed point, i.e., $dg/dl = 0$, with l the RG-flow parameter. In other words, the continuum limit of H_1 is a scale-invariant quantum field theory in $(1+1)$ dimensions. In combination with unitarity, a theorem by Zamolodchikov and Polchinski [35] implies that this is indeed a $(1+1)$-dimensional conformal field theory (CFT).[3] Therefore, we expect a critical behavior in the numerical simulations of the lattice Hamiltonian for a purely chiral ladder in Eq. (1).

At this point, it is worth mentioning that, using these results for the continuum limit, we can actually predict some of the expected behavior for the correlation functions that we will compute for the lattice model. In particular, let us consider here the spin-spin correlator $\langle \mathbf{S}_i \mathbf{S}_j \rangle$ for, say, the upper leg. Rewriting the continuum limit of spin operators as in Eq. (B9), one arrives at a expression for the correlator in terms of $\mathbf{J}_{L/R}$ and $\mathbf{n}$ fields. Using the operator product expansion for these fields, one can compute the decay of the asymptotic decay of the correlator. These operator product expansions can be found in, e.g., the Appendix of Ref. [11]. The relevant nonvanishing ones for our case are

$$J_M^a(x_M)J_M^b(0) \sim \frac{1}{(2\pi)^2}\frac{\delta_{ab}/2}{x_M^2} + \frac{i\epsilon_{abc}}{2\pi}\frac{J_R^c(0)}{x_M},$$

$$n^a(x)n^b(0) \sim \frac{1}{2\pi^2 a}\frac{\delta_{ab}}{(x_L x_R)^{1/2}},$$

$$J_L^a(x_L)n^b(0) \sim i\frac{\epsilon_{abc}n^c(0) + \delta_{ab}\text{tr}(g(0))/2\pi a}{4\pi x_L},$$

$$J_R^a(x_R)n^b(0) \sim i\frac{\epsilon_{abc}n^c(0) - \delta_{ab}\text{tr}(g(0))/2\pi a}{4\pi x_R}, \tag{B11}$$

---

[3]As far as the authors know, this theorem only exists for two-dimensional CFTs, and its generalization to higher dimensions has proven remarkably hard.
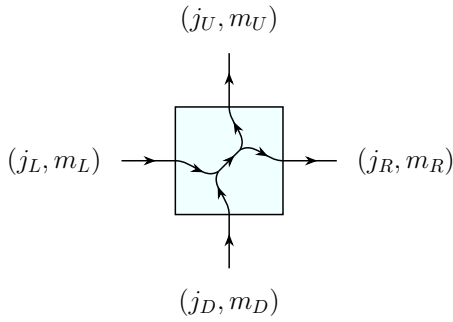
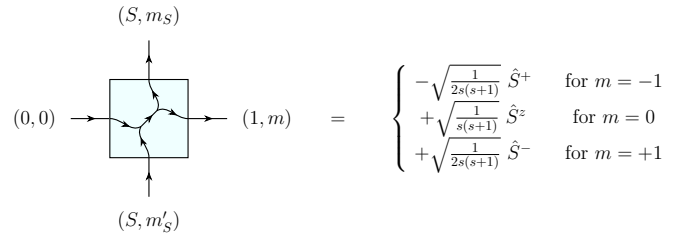FIG. 17. Internal SU(2) structure of a generic MPO tensor with four indices.

FIG. 18. Matrices for the MPO tensor with the left bond index fixed to spin-0 and the right bond index fixed to spin-1, leaving the freedom of choosing $m = -1, 0, +1$. Physical indices have spin $S = \frac{1}{2}$.

with $M = L/R$ and $x_{L/R} = v\tau \pm ix$ holonomic/antiholonomic coordinates (where τ is imaginary time and v the velocity of the spin mode). Expanding the correlator and computing the vacuum expectation value according to the above expressions, the leading contribution at long distances is given by $\sum_a n^a(x)n^a(0)$, such that we obtain

$$\langle \mathbf{S}_i \mathbf{S}_j \rangle \propto \frac{1}{|j - i|} \tag{B12}$$

up to multiplicative and additive constants. We will confirm this asymptotic decay later with our numerical simulations, as well as compute a number of other lattice correlation functions.

APPENDIX C: CONSTRUCTION OF SU(2)-INVARIANT MPOS

Here, we explain how to construct MPOs for different types of SU(2)-invariant interactions based on symmetry considerations only. We start with simple MPOs, such as the one for the Heisenberg quantum spin chain, and then move on to more complex interactions such as the three-spin chiral interactions that we consider in this paper.

The ultimate goal is to write the desired Hamiltonian in an SU(2)-invariant form, which implies a decomposition in terms of degeneracy tensors and structural tensors (Clebsch-Gordan coefficients) as described by the Wigner-Eckart theorem. In order to do this, we first consider the Clebsch-Gordan coefficients which are eligible for the MPO and determine afterward which degeneracy factors are necessary in order to construct the correct Hamiltonian, with the constraint that the Hamiltonian must be an SU(2) scalar.

As a building block, we consider the generic MPO tensor in Fig. 17, which shows an internal structure due to the presence of four indices in the MPO tensor. The left/right indices are the MPO bond indices, and the up/down indices are the physical indices. Each trivalent tensor corresponds to an intertwiner of SU(2), i.e., a Clebsch-Gordan coefficient. Arrows show the direction of the legs (incoming/outgoing irreps, see Ref. [9]).

To show how the construction process works for the MPO, we consider two different Hamiltonians: a two-site Heisenberg interaction $\mathbf{S} \cdot \mathbf{S}$, and a three-spin chiral interaction $\mathbf{S} \cdot (\mathbf{S} \times \mathbf{S})$.

1. Heisenberg two-spin interaction

Since the term $\mathbf{S} \cdot \mathbf{S}$ produces a scalar, we are interested in MPOs that transform as a scalar as well, which means that the bond indices at the left and right ends of the MPO need to have spin-0. For two physical spins-$\frac{1}{2}$, it is easy to check that this implies that the connecting bond index between two MPO sites can only have either spin-0 or spin-1. While the spin-0 channel is trivial and corresponds to the application of the identity operator on the physical spins, the spin-1 channel *necessarily* generates the dot product. This is because the only two scalar operators for two spins are $\mathbb{I} \otimes \mathbb{I}$ and $\mathbf{S} \cdot \mathbf{S} \equiv S^x \otimes S^x + S^y \otimes S^y + S^z \otimes S^z$. For the left and right MPO tensors, we can now write all the coefficients once all the irreducible representations are fixed. Focusing on the spin-1 channel for the connecting index, the results are shown in Figs. 18 and 19. It is then straightforward to check that the contraction of the left and right MPO tensors from Figs. 18 and 19 gives back the desired dot product $\mathbf{S} \cdot \mathbf{S}$ of the two-site Heisenberg Hamiltonian, with a prefactor of $-\frac{4}{3}$ as shown in Fig. 20.

Next, we can easily build the SU(2)-invariant MPO for the Heisenberg quantum spin chain with $H = \sum_i \mathbf{S}_i \cdot \mathbf{S}_{i+1}$ by adding one more spin-0 channel to the MPO bond index. More specifically, the irrep with spin-0 will have degeneracy two, i.e., we will have 0_1 and 0_2 (the subscript refers to the degeneracy). Combined with the nondegenerate spin channel 1_1, the MPO can be written according to Fig. 21, where we show the details of the degeneracy tensors accompanying the structural (Clebsch-Gordan) part. As in the nonsymmetric part, the irrep 0_1 "propagates" through the bond indices until an interaction
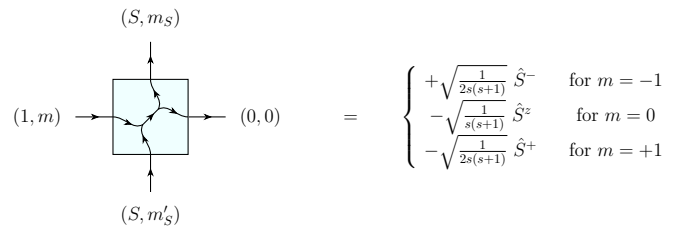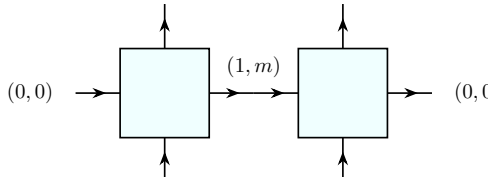

FIG. 19. Matrices for the MPO tensor with the left bond index fixed to spin-1 and the right bond index fixed to spin-0, leaving the freedom of choosing $m = -1, 0, +1$. Physical indices have spin $S = \frac{1}{2}$.

$$= -\left(\sqrt{\tfrac{2}{3}}\right)^2 S_i^+ S_{i+1}^- - \left(\tfrac{2}{\sqrt{3}}\right)^2 S_i^z S_{i+1}^z - \left(\sqrt{\tfrac{2}{3}}\right)^2 S_i^- S_{i+1}^+ = -\tfrac{4}{3}\vec{S}_i \cdot \vec{S}_{i+1}$$

FIG. 20. The contraction of the MPO tensors in Figs. 18 and 19 produces the desired two-site Heisenberg interaction with a $-\tfrac{4}{3}$ prefactor. The sum is over the values of m for the spin-1 channel of the bond index.

is hit (which is mediated by irrep 1), and onwards propagates the irrep 0_2. In describing this MPO tensor we have used the notation

$$\vec{S} = \left(-\sqrt{\tfrac{2}{3}}S^+, \tfrac{2}{\sqrt{3}}S^z, \sqrt{\tfrac{2}{3}}S^-, \right), \quad \vec{\bar{S}} = \begin{pmatrix} \sqrt{\tfrac{2}{3}}S^- \\ -\tfrac{2}{\sqrt{3}}S^z \\ -\sqrt{\tfrac{2}{3}}S^+ \end{pmatrix},$$

(C1)

for a system of spin-$\tfrac{1}{2}$. Moreover, we also defined the factor $\gamma \equiv i\sqrt{3/4}$ that compensates the unavoidable factor $-\tfrac{4}{3}$, which appears due to the contraction of the Clebsch-Gordan tensors as shown in Fig. 20.
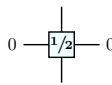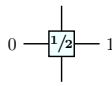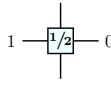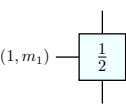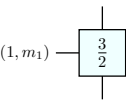

FIG. 21. MPO tensor with SU(2) symmetry for the Heisenberg quantum spin chain. The degeneracy tensors go together with the rank-4 structural tensor for the spin sectors shown. All other spin sectors have vanishing degeneracy tensors. The internal spin for every block is shown in bold font, the physical spin is always $S = \tfrac{1}{2}$. The labels of the MPO indices are in the order D, L, R, U.

FIG. 22. Possible coefficients of the central MPO tensor for the scalar triple product. Here, the internal leg of the MPO can have the two spin representations $\tfrac{1}{2}$ and $\tfrac{3}{2}$.

2. Chiral three-spin interaction

As a second example of a scalar operator we consider the triple product $\mathbf{S} \cdot (\mathbf{S} \times \mathbf{S})$. In this case, the MPO spans over three sites. The interaction on the second site can only be mediated by having a spin-1 representation on both virtual legs of the central MPO tensor. If this tensor had a spin-0 representation on either leg, then it would not be possible to generate a three-body interaction. Moreover, a spin-2 representation is excluded since the three-site MPO can then no longer be terminated by a spin-0 after the third site, which we demand in order for it to be a scalar. Additionally, the central MPO tensor will have different internal spin-$\tfrac{1}{2}$ and/or spin-$\tfrac{3}{2}$, since

$$\tfrac{1}{2} \otimes 1 = \tfrac{1}{2} \oplus \tfrac{3}{2},$$

(C2)

where spin-1 will come from some bond index, and spin-$\tfrac{1}{2}$ from some physical index.

In order to start and terminate the interaction in the MPO, we can reuse the terms of the Heisenberg interaction from Figs. 18 and 19. The additional terms of the MPO for the triple product can be again constructed by evaluating the Clebsch-Gordan coefficients for fixed spin representations of the virtual legs for the central MPO tensor. These are given explicitly in Fig. 22, for the two possible values $\tfrac{1}{2}$ and $\tfrac{3}{2}$ of the internal leg.

In order to construct the MPO, we can now take linear combinations of matrices A and B in Fig. 22 together with the left and right tensors from Figs. 18 and 19. This is shown in Fig. 23. We also use the notation

$$\overset{\leftrightarrow}{M} = \alpha \overset{\leftrightarrow}{A} + \beta \overset{\leftrightarrow}{B}.$$

(C3)
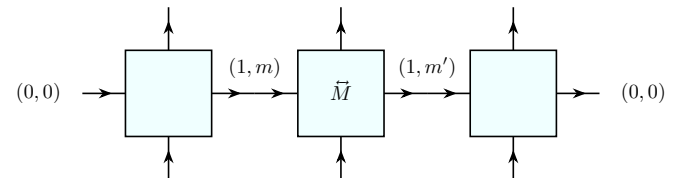
FIG. 23. General construction of a three-site MPO with the linear combination $\overset{\leftrightarrow}{M} = \alpha \overset{\leftrightarrow}{A} + \beta \overset{\leftrightarrow}{B}$. Summation over the common indices m and m' is assumed.

$$\text{full MPO} = \begin{array}{c} \\ 0_1 \\ 1_1 \\ 1_2 \\ 0_2 \end{array} \overset{\begin{array}{cccc} 0_1 & 1_1 & 1_2 & 0_2 \end{array}}{\begin{pmatrix} \mathbb{I} & \gamma\overleftarrow{S} & 0 & 0 \\ 0 & 0 & \overleftrightarrow{M} & J\gamma\vec{S} \\ 0 & 0 & 0 & K\gamma\vec{S} \\ 0 & 0 & 0 & \mathbb{I} \end{pmatrix}}$$

chargeSector j_{int} j_1 j_2 j_3 j_4	dimensionality	degeneracyTensor	MPO
$\frac{1}{2}$ $\frac{1}{2}$ 0 0 $\frac{1}{2}$	[1, 2, 2, 1]	$\begin{array}{c}\\ 0_1\\ 0_2\end{array}\overset{\begin{array}{cc}0_1 & 0_2\end{array}}{\begin{pmatrix}1 & 0\\ 0 & 1\end{pmatrix}}$	0 —[1/2]— 0
$\frac{1}{2}$ $\frac{1}{2}$ 0 1 $\frac{1}{2}$	[1, 2, 2, 1]	$\begin{array}{c}\\ 0_1\\ 0_2\end{array}\overset{\begin{array}{cc}1_1 & 1_2\end{array}}{\begin{pmatrix}\gamma & 0\\ 0 & 0\end{pmatrix}}$	0 —[1/2]— 1
$\frac{1}{2}$ $\frac{1}{2}$ 1 0 $\frac{1}{2}$	[1, 2, 2, 1]	$\begin{array}{c}\\ 1_1\\ 1_2\end{array}\overset{\begin{array}{cc}0_1 & 0_2\end{array}}{\begin{pmatrix}0 & J\gamma\\ 0 & K\gamma\end{pmatrix}}$	1 —[1/2]— 0
$\frac{1}{2}$ $\frac{1}{2}$ 1 1 $\frac{1}{2}$	[1, 2, 2, 1]	$\begin{array}{c}\\ 1_1\\ 1_2\end{array}\overset{\begin{array}{cc}1_1 & 1_2\end{array}}{\begin{pmatrix}0 & \alpha\\ 0 & 0\end{pmatrix}}$	1 —[1/2]— 1
$\frac{3}{2}$ $\frac{1}{2}$ 1 1 $\frac{1}{2}$	[1, 2, 2, 1]	$\begin{array}{c}\\ 1_1\\ 1_2\end{array}\overset{\begin{array}{cc}1_1 & 1_2\end{array}}{\begin{pmatrix}0 & \beta\\ 0 & 0\end{pmatrix}}$	1 —[3/2]— 1

FIG. 24. MPO tensor with SU(2) symmetry for the quantum spin chain Heisenberg and chiral three-spin interactions. The degeneracy tensors go together with the rank-4 structural tensor for the spin sectors shown. All other spin sectors have vanishing degeneracy tensors. The operator $\overleftrightarrow{M}$ is the combination of the operators $\overleftrightarrow{A}$ and $\overleftrightarrow{B}$ with proper weights. Again, the labels of the MPO indices are in the order D, L, R, U.

Here the arrowheads indicate the center site of the MPO, in analogy to Fig. 21, where arrows were used to signal the start and end of the interaction.

The free parameters α and β can now be chosen in order to reproduce the desired interaction. As a first option, one could choose the superposition $-A + B$. For this choice, the MPO tensor at the central site simplifies to

$$-A + B = \begin{pmatrix} \mathbb{I} & 0 & 0 \\ 0 & \mathbb{I} & 0 \\ 0 & 0 & \mathbb{I} \end{pmatrix}, \tag{C4}$$

such that the overall three-body MPO reproduces a next-to-nearest-neighbor Heisenberg interaction $\mathbf{S_1} \cdot \mathbf{S_3}$ instead of the scalar triple product we aim for. As a matter of fact, this is also a valid scalar for three spins, where the second spin simply does not interact. By playing with this choice of α and β it is also possible to construct MPOs for long-range interactions. In our case, though, we find that in order to generate the chiral triple product, it is necessary to choose $\alpha = -i$ and $\beta = -i/2$,

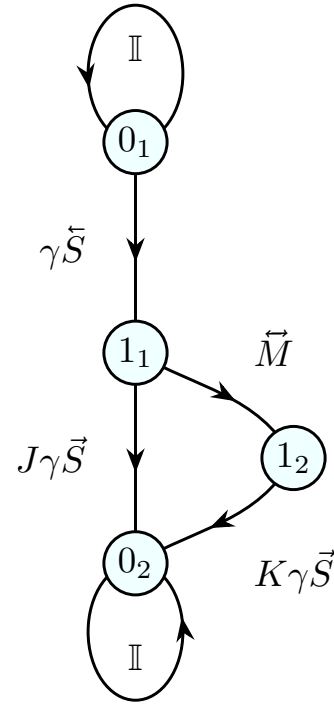
FIG. 25. Finite state machine for the MPO of the spin-$\frac{1}{2}$ nearest-neighbor Heisenberg model with chiral three-spin interactions. The different states correspond to the different spin sectors for the bond dimensions of the MPO.

in which case the MPO tensor at the central site becomes

$$-i\left(A + \frac{1}{2}B\right) = i\begin{pmatrix} -S^z & -\frac{\sqrt{2}}{2}S^- & 0 \\ -\frac{\sqrt{2}}{2}S^+ & 0 & -\frac{\sqrt{2}}{2}S^- \\ 0 & -\frac{\sqrt{2}}{2}S^+ & S^z \end{pmatrix}. \tag{C5}$$

Evaluating the sum over the three MPO tensors in Fig. 23 yields

$$\begin{aligned} H &= -\frac{4i}{6}(S^zS^+S^- - S^zS^-S^+ + S^+S^-S^z \\ &\quad - S^+S^zS^- + S^-S^zS^+ - S^-S^+S^z) \\ &= -\frac{4}{3}\mathbf{S}_1 \cdot (\mathbf{S}_2 \times \mathbf{S}_3). \end{aligned} \tag{C6}$$

Notice that here again the factor $-\frac{4}{3}$ appears due to the relation between spin-$\frac{1}{2}$ operators and Clebsch-Gordan coefficients. From these tensors it is then easy to construct an
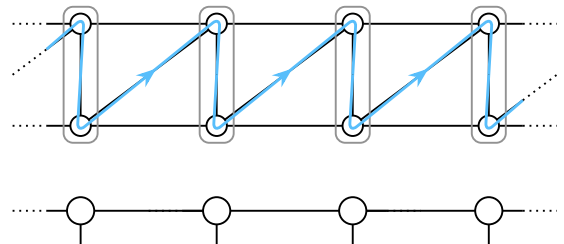

FIG. 26. Snake pattern for the MPO and also coarse graining of two ladder sites into one site of the MPS.
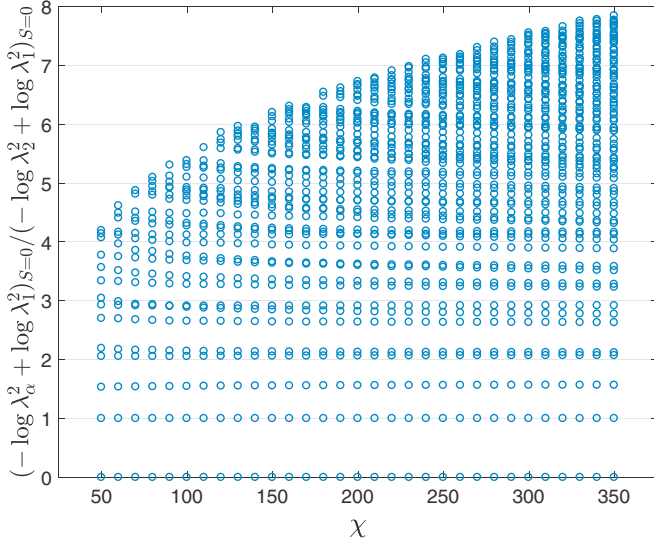
FIG. 27. Scaling of the entanglement spectrum for $S = 0$ with the MPS symmetric bond dimension χ, in normalized units.

MPO for a Hamiltonian made of a sum of chiral three-spin interactions.

3. Two-spin and three-spin interactions together

We can now construct an MPO for a Hamiltonian such as

$$H = J \sum_i \mathbf{S}_i \mathbf{S}_{i+1} + K \sum_i \mathbf{S}_i \cdot (\mathbf{S}_{i+1} \times \mathbf{S}_{i+2}), \qquad \text{(C7)}$$

i.e., a sum of two-spin Heisenberg interactions and chiral three-spin interactions. This Hamiltonian is an SU(2) scalar because it is constructed as a sum of scalar operators. J and K are parameters giving more weight to one term or the other.

As in the case of the plain Heisenberg model, we need two spin-0 sectors in the bond dimensions of the MPO that take care of applying the identity to all sites to the left and
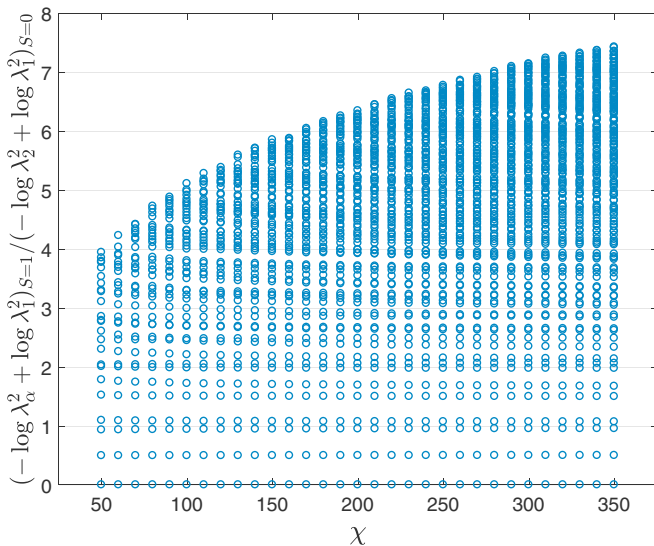
to the right of the interacting sites. Moreover, here we also need two spin-1 sectors in the MPO bond dimension: one mediating the two-spin interaction, and the other mediating the three-spin interaction. The resulting MPO tensor is given in Fig. 24, where we specify the structural part, corresponding to the Clebsch-Gordan coefficients, as well as the degeneracy part. The structure of the MPO can also be represented by a *finite state machine*, as shown in Fig. 25.

4. Chiral three-spin interactions on the ladder

For the purposes of this paper, we simulated a Hamiltonian with chiral three-spin interactions of the triangles of the ladder in Fig. 1, in which we considered alternating orientations for the triangles as explained above. In order to construct an MPO, we considered the snake pattern from Fig. 26, and
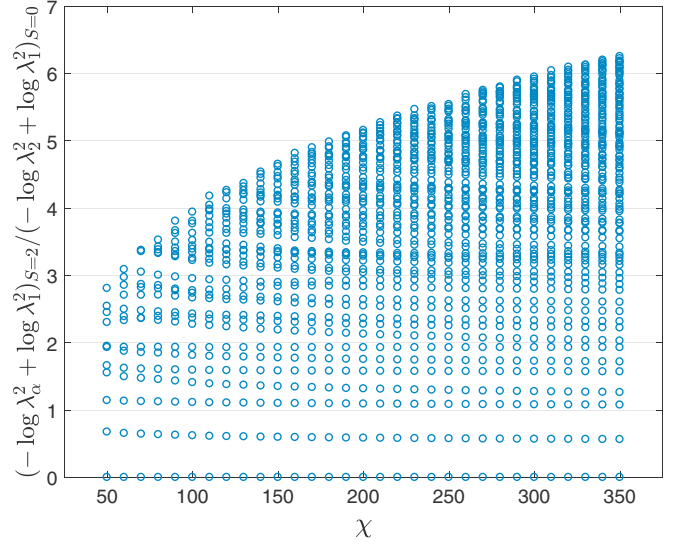

FIG. 29. Scaling of the entanglement spectrum for $S = 2$ with the MPS symmetric bond dimension χ, in normalized units.

FIG. 28. Scaling of the entanglement spectrum for $S = 1$ with the MPS symmetric bond dimension χ, in normalized units.
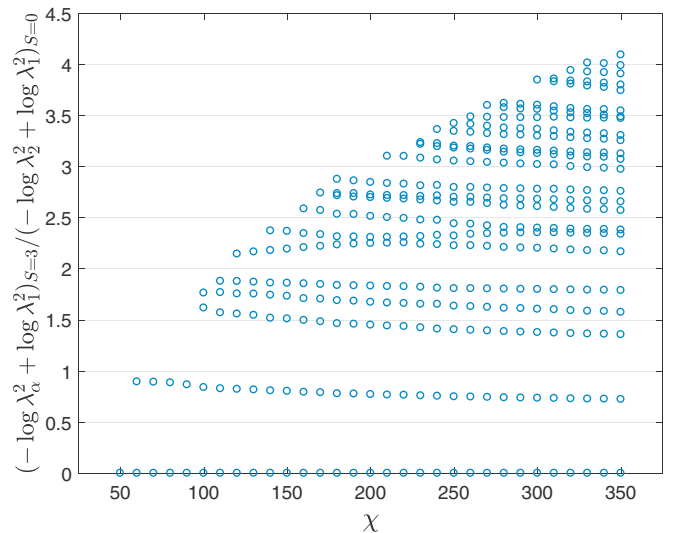

FIG. 30. Scaling of the entanglement spectrum for $S = 3$ with the MPS symmetric bond dimension χ, in normalized units.

applied the techniques discussed previously to construct an MPO for the sum of the different three-spin interactions. Then, as shown in the figure, we coarse grained the two spins for each rung of the ladder into a single physical site (with irreps $0_1 \oplus 1_1$). In this way, the resulting MPO has a two-site unit cell and is the one used in the iDMRG algorithm with a two-site update.

APPENDIX D: FINITE-ENTANGLEMENT SCALING OF THE ENTANGLEMENT SPECTRUM

In this Appendix we show our results for the scaling with the bond dimension χ of the entanglement spectrum for the different spin sectors S. Our results are shown in Figs. 27–30 for integer spins $S = 0$ up to $S = 3$. Each dot in the plots is a $(2S + 1)$-plet. As we can see, the lowest part of the entanglement spectrum converges quickly with the bond dimension. The distribution of the lowest-lying entanglement energies tends to have an equidistant structure, typical of a CFT. The

values for the largest possible bond dimension, which we take as essentially converged for the lowest-lying part of the spectrum, correspond to the ones shown in Fig. 15. We also notice that the convergence of the individual entanglement energies with the symmetric bond dimension seems to be algebraic as opposed to exponential. In practice, this means that from our plots one can extract the behavior

$$\varepsilon_\alpha \approx \frac{1}{\chi^\mu}, \tag{D1}$$

for the αth entanglement energy ε_α, with μ an exponent controlling the behavior at large χ. According to our data, the exponent μ may depend on the index α itself, i.e., be different for each one of the entanglement energies. Even if purely empirical, this behavior seems to hold well for all the studied values of the spin S. According to the results presented in this paper, we take this also as a strong indication that the system is critical and has an infinite correlation length.

[1] S. R. White, Phys. Rev. Lett. **69**, 2863 (1992); Phys. Rev. B **48**, 10345 (1993).

[2] M. Fannes, B. Nachtergaele, and R. F. Werner, Commun. Math. Phys. **144**, 443 (1992); A. Klümper, A. Schadschneider, and J. Zittartz, J. Phys. A: Math. Gen. **24**, L955 (1991); Europhys. Lett. **24**, 293 (1993).

[3] R. Orús, Ann. Phys. (NY) **349**, 117 (2014); Eur. Phys. J. B **87**, 280 (2014).

[4] G. Vidal, Phys. Rev. Lett. **99**, 220405 (2007).

[5] Y.-Y. Shi, L.-M. Duan, and G. Vidal, Phys. Rev. A **74**, 022320 (2006); L. Tagliacozzo, G. Evenbly, and G. Vidal, Phys. Rev. B **80**, 235127 (2009); P. Silvi, V. Giovannetti, S. Montangero, M. Rizzi, J. I. Cirac, and R. Fazio, Phys. Rev. A **81**, 062335 (2010); V. Murg, F. Verstraete, Ö. Legeza, and R. M. Noack, Phys. Rev. B **82**, 205105 (2010).

[6] I. P. McCulloch, arXiv:0804.2509; G. M. Crosswhite, A. C. Doherty, and G. Vidal, Phys. Rev. B **78**, 035116 (2008).

[7] L. Tagliacozzo, T. R. de Oliveira, S. Iblisdir, and J. I. Latorre, Phys. Rev. B **78**, 024410 (2008); F. Pollmann, S. Mukerjee, A. M. Turner, and J. E. Moore, Phys. Rev. Lett. **102**, 255701 (2009).

[8] I. McCulloch and M. Gulacsi, Eur. Phys. Lett. **57**, 852 (2002); S. Singh, H.-Q. Zhou, and G. Vidal, New J. Phys. **12**, 033029 (2010).

[9] P. Schmoll, S. Singh, M. Rizzi, and R. Orús, arXiv:1809.08180.

[10] B. Bauer, L. Cincio, B. P. Keller, M. Dolfi, G. Vidal, S. Trebst, and A. W. W. Ludwig, Nat. Commun. **5**, 5137 (2014).

[11] P.-H. Huang, J.-H. Chen, A. E. Feiguin, C. Chamon, and C. Mudry, Phys. Rev. B **95**, 144413 (2017).

[12] P. Lecheminant and A. M. Tsvelik, Phys. Rev. B **95**, 140406(R) (2017).

[13] G. Gorohovsky, R. G. Pereira, and E. Sela, Phys. Rev. B **91**, 245139 (2015).

[14] C. L. Kane, R. Mukhopadhyay, and T. C. Lubensky, Phys. Rev. Lett. **88**, 036401 (2002); J. C. Y. Teo and C. L. Kane, Phys. Rev. B **89**, 085101 (2014); J. Klinovaja and D. Loss, Phys. Rev. Lett. **112**, 246403 (2014); Y. Oreg, E. Sela, and A. Stern, Phys. Rev.

B **89**, 115402 (2014); E. Sagi and Y. Oreg, ibid. **90**, 201102(R) (2014); T. Neupert, C. Chamon, C. Mudry, and R. Thomale, ibid. **90**, 205101 (2014).

[15] S. T. Carr, B. N. Narozhny, and A. A. Nersesyan, Phys. Rev. B **73**, 195114 (2006); E. M. Stoudenmire, J. Alicea, O. A. Starykh, and M. P. A. Fisher, ibid. **84**, 014503 (2011); C.-W. Huang, S. T. Carr, D. Gutman, E. Shimshoni, and A. D. Mirlin, ibid. **88**, 125134 (2013); A. Petrescu, M. Piraud, G. Roux, I. P. McCulloch, K. Le Hur, ibid. **96**, 014524 (2017); R. A. Santos and B. Béri, arXiv:1806.02874; S. Rachel, Rep. Prog. Phys. **81**, 116501 (2018).

[16] N. R. Cooper, J. Dalibard, I. B. Spielman, arXiv:1803.00249; S. Barbarino, L. Taddia, D. Rossini, L. Mazza, and R. Fazio, New J. Phys. **18**, 035010 (2016); L. Taddia, E. Cornfeld, D. Rossini, L. Mazza, E. Sela, and R. Fazio, Phys. Rev. Lett. **118**, 230402 (2017); M. Atala, M. Aidelsburger, M. Lohse, J. T. Barreiro, B. Paredes, and I. Bloch, Nat. Phys. **10**, 588 (2014); M. Mancini, G. Pagano, G. Cappellini, L. Livi, M. Rider, J. Catani, C. Sias, P. Zoller, M. Inguscio, M. Dalmonte, and L. Fallani, Science **349**, 1510 (2015); B. K. Stuhl, H.-I. Lu, L. M. Aycock, D. Genkina, and I. B. Spielman, ibid. **349**, 1514 (2015); M. L. Wall, A. P. Koller, S. Li, X. Zhang, N. R. Cooper, J. Ye, and A. M. Rey, Phys. Rev. Lett. **116**, 035301 (2016); L. F. Livi, G. Cappellini, M. Diem, L. Franchi, C. Clivati, M. Frittelli, F. Levi, D. Calonico, J. Catani, M. Inguscio, and L. Fallani, ibid. **117**, 220401 (2016); J. H. Han, J. H. Kang, and Y. Shin, **122**, 065303 (2019); J. H. Kang, J. H. Han, and Y. Shin, ibid. **121**, 150403 (2018).

[17] T. Giamarchi, *Quantum Physics in One Dimension* (Clarendon, Oxford, 2003).

[18] A. O. Gogolin, A. A. Nersesyan, and A. M. Tsvelik, *Bosonization and Strongly Correlated Systems* (Cambridge University Press, Cambridge, 1998).

[19] T. Keilmann, S. Lanzmich, I. McCulloch, and M. Roncaglia, Nat. Commun. **2**, 361 (2011); S. Greschner, G. Sun, D. Poletti, and L. Santos, Phys. Rev. Lett. **113**, 215303 (2014); S. Greschner and L. Santos, ibid. **115**, 053002 (2015); A. Bermudez and D. Porras, New J. Phys. **17**, 103021 (2015).

[20] F. Görg, K. Sandholzer, J. Minguzzi, R. Desbuquois, M. Messer, and T. Esslinger, arXiv:1812.05895.

[21] K. Zapp and R. Orús, Phys. Rev. D **95**, 114508 (2017).

[22] P. Corboz, Phys. Rev. B **93**, 045116 (2016).

[23] U. Schollwöck, Rev. Mod. Phys. **77**, 259 (2005).

[24] C. Holzhey, F. Larsen, and F. Wilczek, Nucl. Phys. B **424**, 443 (1994); G. Vidal, J. I. Latorre, E. Rico, and A. Kitaev, Phys. Rev. Lett. **90**, 227902 (2003); J. I. Latorre, E. Rico, and G. Vidal, Quantum Inf. Comput. **4**, 48 (2004); P. Calabrese and J. Cardy, J. Stat. Mech. (2004) P06002.

[25] T. Vekua and G. Sun, Phys. Rev. B **94**, 014417 (2016).

[26] I. Affleck, D. Gepner, H. J. Schulz, and T. Ziman, J. Phys. A: Math. Gen. **22**, 511 (1989).

[27] J. Cardy and E. Tonni, J. Stat. Mech. (2016) 123103.

[28] F. Verstraete and J. I. Cirac, arXiv:cond-mat/0407066.

[29] J. Jordan, R. Orús, G. Vidal, F. Verstraete, and J. I. Cirac, Phys. Rev. Lett. **101**, 250602 (2008).

[30] T. Liu, W. Li, A. Weichselbaum, J. von Delft, and G. Su, Phys. Rev. B **91**, 060403(R) (2015); W. Li, A. Weichselbaum, J. von Delft, and H.-H. Tu, *ibid.* **91**, 224414 (2015); S.-J. Ran, W. Li, S.-S. Gong, A. Weichselbaum, J. von Delft, and G. Su, *ibid.* **97**, 075146 (2018); M. Mambrini, R. Orús, and D. Poilblanc, *ibid.* **94**, 205124 (2016); D. Poilblanc and M. Mambrini, *ibid.* **96**, 014414 (2017); J.-Y. Chen, L. Vanderstraeten, S. Capponi, and D. Poilblanc, *ibid.* **98**, 184409 (2018).

[31] I. Affleck and F. D. M. Haldane, Phys. Rev. B **36**, 5291 (1987).

[32] M. B. Kruger and C. Meade, Phys. Rev. B **55**, 1 (1997).

[33] I. Affleck, Les Houches Lecture Notes, Session XLIX, *Fields, Strings and Critical Phenomena* (Elsevier, Amsterdam, 1989).

[34] J.-H. Chen, C. Mudry, C. Chamon, and A. M. Tsvelik, arXiv:1810.09858.

[35] A. B. Zamolodchikov, JETP Lett. **43**, 730 (1986) [Pisma Zh. Eksp. Teor. Fiz. **43**, 565 (1986)]; J. Polchinski, Nucl. Phys. B **303**, 226 (1988).